



# Fusarium fruiting body microbiome member *Pantoea agglomerans* inhibits fungal pathogenesis by targeting lipid rafts

Sunde Xu<sup>1,7</sup>, Yong-Xin Liu<sup>ID 2,7</sup>, Tomislav Cernava<sup>3,7</sup>, Hongkai Wang<sup>1</sup>, Yaqi Zhou<sup>1</sup>, Tie Xia<sup>4</sup>, Shugeng Cao<sup>5</sup>, Gabriele Berg<sup>3</sup>, Xing-Xing Shen<sup>ID 1</sup>, Ziyue Wen<sup>1</sup>, Chunshun Li<sup>5</sup>, Baoyuan Qu<sup>2</sup>, Hefei Ruan<sup>4</sup>, Yunrong Chai<sup>ID 6</sup>, Xueping Zhou<sup>ID 1</sup>, Zhonghua Ma<sup>1</sup>, Yan Shi<sup>ID 4</sup>, Yunlong Yu<sup>ID 1✉</sup>, Yang Bai<sup>ID 2✉</sup> and Yun Chen<sup>ID 1✉</sup>

Plant-pathogenic fungi form intimate interactions with their associated bacterial microbiota during their entire life cycle. However, little is known about the structure, functions and interaction mechanisms of bacterial communities associated with fungal fruiting bodies (perithecia). Here we examined the bacterial microbiome of perithecia formed by *Fusarium graminearum*, the major pathogenic fungus causing Fusarium head blight in cereals. A total of 111 shared bacterial taxa were identified in the microbiome of 65 perithecium samples collected from 13 geographic locations. Within a representative culture collection, 113 isolates exhibited antagonistic activity against *F. graminearum*, with *Pantoea agglomerans* ZJU23 being the most efficient in reducing fungal growth and infectivity. Herbicolin A was identified as the key antifungal compound secreted by ZJU23. Genetic and chemical approaches led to the discovery of its biosynthetic gene cluster. Herbicolin A showed potent *in vitro* and *in planta* efficacy towards various fungal pathogens and fungicide-resistant isolates, and exerted a fungus-specific mode of action by directly binding and disrupting ergosterol-containing lipid rafts. Furthermore, herbicolin A exhibited substantially higher activity (between 5- and 141-fold higher) against the human opportunistic fungal pathogens *Aspergillus fumigatus* and *Candida albicans* in comparison with the clinically used fungicides amphotericin B and fluconazole. Its mode of action, which is distinct from that of other antifungal drugs, and its efficacy make herbicolin A a promising antifungal drug to combat devastating fungal pathogens, both in agricultural and clinical settings.

The microbiome plays a crucial role in host development, fitness and health<sup>1–4</sup>. Numerous microbiome studies have provided insights into the composition of various microbial communities and their dynamic changes in response to exogenous factors<sup>5–8</sup>. However, autogenic factors in microbiome assembly and function are mostly overlooked, especially in terms of the importance of microbe–microbe interactions<sup>1</sup>. Detailed knowledge of physical and molecular interactions between different microbiome members has a high potential to aid the development of new strategies for targeted manipulations of the microbiome to improve host health<sup>3,4,9,10</sup>. In addition, the underlying interactions could also be considered in a broader sense for microbial communities of pathogenic host organisms, for example phytopathogenic fungi.

Interactions between bacteria and fungi are crucial for modulating microbial communities in terms of biodiversity, ecosystem functions and host health when associated with multicellular organisms<sup>11</sup>. Molecular mechanisms governing inter-kingdom communication are reflected by numerous biological interactions, from antagonism to mutualism<sup>12</sup>. In agroecosystems, investigations of bacterial–fungal interactions are mainly focused on the suppression

of pathogens<sup>4,12,13</sup>. Bacteria generally interfere with fungal pathogens by competition for resources and secretion of lytic enzymes or bioactive compounds (antibiosis)<sup>14</sup>. In most cases, the detailed modes of action of many antagonistic bacterial–fungal interactions and the involved bioactive compounds remain elusive<sup>15</sup>. Sometimes the underlying mechanisms have been only partially deciphered. For example, herbicolin A, which can be biosynthesized by certain *Pantoea agglomerans* isolates, was identified about 40 years ago as the bacterium’s most important bioactive compound against fungi and Mollicutes<sup>16–21</sup>. However, the structure of the biosynthetic gene cluster for herbicolin A as well as its mode of action remain elusive.

Most phytopathogenic fungi can produce sexual structures such as perithecia that allow them to survive on infested plant debris before the next infection cycle<sup>22</sup>. *Fusarium graminearum* (Fg), the major pathogen causing Fusarium head blight (FHB) in wheat (*Triticum aestivum*), uses this strategy with high efficiency<sup>23</sup>. FHB epidemics not only affect global wheat production, but also contaminate grain with mycotoxins<sup>24</sup>. Interfering with perithecium formation to decrease the initial inoculum is a potential strategy for FHB management. Current literature mostly focuses

<sup>1</sup>State Key Laboratory of Rice Biology, Key Laboratory of Molecular Biology of Crop Pathogens and Insects, Department of Plant Protection, Zhejiang University, Hangzhou, China. <sup>2</sup>State Key Laboratory of Plant Genomics, CAS-JIC Centre of Excellence for Plant and Microbial Science, Institute of Genetics and Developmental Biology, Innovation Academy for Seed Design, Chinese Academy of Sciences, Beijing, China. <sup>3</sup>Institute of Environmental Biotechnology, Graz University of Technology, Graz, Austria. <sup>4</sup>Institute for Immunology, Department of Basic Medical Sciences, Center for Life Sciences, Tsinghua University, Beijing, China. <sup>5</sup>Department of Pharmaceutical Sciences, University of Hawaii, Hilo, HI, USA. <sup>6</sup>Department of Biology, Northeastern University, Boston, MA, USA. <sup>7</sup>These authors contributed equally: Sunde Xu, Yong-Xin Liu, Tomislav Cernava. ✉e-mail: [ylyu@zju.edu.cn](mailto:ylyu@zju.edu.cn); [ybai@genetics.ac.cn](mailto:ybai@genetics.ac.cn); [chenyun0927@zju.edu.cn](mailto:chenyun0927@zju.edu.cn)

on changes of the plant microbiome as a response to disease or contrasts healthy with diseased states<sup>4,25–27</sup>. The initial origin of disease-responsive microorganisms remains in most cases elusive; they might be associated with the plant host or with the pathogen itself. Similar to soil, plants and animals, fungal structures are also known to provide microhabitats for adapted bacterial communities; they can also be involved in destructive interactions with their hosts. Perithecia provide a highly specific ecological niche for bacteria that we hypothesized could play a pivotal role in disease establishment. Preliminary assessments of bacterial–fungal interactions in such microhabitats indicated antagonistic activity via emission of volatile bioactive metabolites<sup>28,29</sup>. At present, there is a lack of large-scale assessments of fungal fruiting body microbiomes and mechanistic insights into interactions between prevalent bacteria and their hosts.

In this study, bacterial communities associated with Fg perithecia were profiled. Phylogenetically distinct bacteria were always detectable in perithecia from separated geographic locations in China. In parallel, representatives of 30 core microbiome members were cultured and screened for antagonistic activity. This resulted in the isolation of one highly active antagonist (*Pantoea agglomerans* ZJU23) with pronounced antagonistic activity against FHB. We showed that herbicin A (HA) secreted by ZJU23 is responsible for suppression of the phytopathogen. HA binds ergosterol and disrupts the integrity of ergosterol-containing fungal lipid rafts suppressing fungal growth, perithecium formation and virulence of Fg. Furthermore, we showed that HA has a wide antifungal spectrum including human opportunistic fungal pathogens, indicating a potential for its use in controlling fungal diseases in agricultural and clinical settings.

## Results

**Insights into perithecium-associated bacterial communities.** Using scanning electron microscopy, morphologically distinct bacteria were found to be embedded in or attached to the surface of Fg perithecia that were collected from geographically distant fields (Fig. 1a and Extended Data Fig. 1a). For a detailed analysis of bacterial communities, we sampled perithecia, rice stubbles and rhizosphere soil from 13 sites within major wheat-growing regions (Fig. 1b and Supplementary Data 1). The bacterial community was profiled on the basis of bacterial 16S ribosomal RNA (rRNA) gene fragment sequences clustered into operational taxonomic units (OTUs; 97% sequence similarity) (Extended Data Fig. 1b). We obtained 49,457,306 high-quality reads from 195 samples (ranging from 5,933 to 547,412 reads, with an average of 253,627 reads per sample), phylogenetically representing 4,912 OTUs (mean: 1,787 OTUs per perithecium sample; 976 OTUs per rice stubble sample; 3,179 OTUs per rhizosphere soil sample; Supplementary Data 2). Rarefaction curves indicated that the sequencing depth of the current study was sufficient to capture bacterial diversity (Extended Data Fig. 2a).

Assessments of  $\alpha$ -diversity revealed a significant difference in richness and Shannon index among perithecium, rice stubble and rhizosphere soil samples (Fig. 1c,d;  $P < 0.05$ , ANOVA, Tukey's HSD). Detailed examination of the bacterial composition of these samples showed that the perithecium microbiota exhibited higher diversity than those found in stubble, but lower diversity than those in rhizosphere soil (Fig. 1c,d). Unconstrained principal coordinate analysis (PCoA), based on a Bray–Curtis distance matrix, revealed that the perithecium communities formed a distinct cluster and indicated that they are more similar to the stubble communities than to the rhizosphere soil communities (Fig. 1e;  $P = 0.001$ , PERMANOVA with Adonis test). Moreover, constrained PCoA (CPCoA) plotting with complementary analyses indicated that the clusters explained 23.3% of the variance within the three compartments (Extended Data Fig. 2b;  $P = 0.001$ , permutation test

with anova.cca). Further analysis based on average Bray–Curtis distances of taxonomic composition at the phylum level across 13 sites revealed that bacterial communities from perithecia, stubble and rhizosphere soil clearly clustered according to the respective compartment (Fig. 1f). Different OTUs visualized in a Manhattan plot showed similar distribution patterns (Extended Data Fig. 2c and Supplementary Data 2). Predominant OTUs (relative abundance  $>0.1\%$ , 111 OTUs) were defined as the core microbiome of perithecia and account for 2.3% (111/4,912) of the total OTUs, and 80.4% and 74.4% relative abundance in the perithecium and stubble microbiomes, respectively. These OTUs were classified into 13 bacterial orders and 32 families, belonging to the phyla Proteobacteria, Actinobacteria, Bacteroidetes and Firmicutes (Fig. 1g). Microbial source tracking analysis revealed that perithecium-associated bacteria mainly originated from the stubble microbiome (mean  $\pm$  s.e.m. fractional contribution,  $92.85 \pm 0.81\%$ ; Extended Data Fig. 2d and Supplementary Data 3). The overall results indicated that the microbiome of perithecia was distinguishable from those of the other analysed compartments.

**ZJU23 isolate reduces FHB and mycotoxin contamination.** To test whether there are beneficial bacteria in the Fg perithecium microbiome for biological control of FHB, we isolated and identified bacteria from 65 independently pooled perithecium samples collected from the aforementioned fields<sup>30</sup> (Extended Data Fig. 1c). A total of 2,036 bacterial isolates were recovered from perithecia, which shared  $>97\%$  16S rRNA gene similarity to 30 OTUs in the core perithecium microbiome (relative abundance  $>0.1\%$ , a total of 111 OTUs) (Fig. 2a and Supplementary Data 2). Among them, 113 isolates representing 13 core OTUs demonstrated various degrees of inhibitory activity against fungal growth in dual-culture assays (Fig. 2a and Supplementary Data 4). Notably, a bacterial isolate (termed ZJU23) showed the strongest inhibitory activity against Fg during co-cultivation, producing radial inhibition zones  $\geq 20$  mm (Fig. 2b). ZJU23 was matched to OTU\_10 in the core perithecium microbiome (Supplementary Data 2), which was identified as *Pantoea agglomerans* on the basis of phylogenetic analysis and genome sequencing. The ZJU23 genome comprises one chromosome and three plasmids (Supplementary Fig. 1).

ZJU23 treatment significantly suppressed perithecium formation, with 80–90% reduction both on carrot (*Daucus carota*) agar plates (Fig. 2c) and rice straws (Extended Data Fig. 3a), in comparison with untreated control and non-antagonistic *P. agglomerans* strain Pa58 treatment. Pa58 isolated from the perithecium microbiome showed similar growth and colonization patterns to ZJU23 and was used as a control to exclude the possibility that nutrient competition is involved in the observed effects (Supplementary Fig. 2). Deoxynivalenol (DON) synthesized in fungal DON-toxisomes is a critical virulence factor of Fg<sup>24,31</sup>. We found that ZJU23 substantially suppressed the formation of fungal DON-toxisomes as indicated by Tri1-GFP in the Fg hyphae grown in the DON induction medium (Fig. 2d). Comparative assessments confirmed that DON production was significantly decreased when Fg was co-cultured with ZJU23 (Fig. 2e). To determine whether ZJU23 inhibited growth of Fg in planta, we conducted biocontrol experiments both in a growth chamber and in the field (see Supplementary Methods for details). Treatment with ZJU23 by foliar spray almost completely suppressed Fg infection on wheat heads (Fig. 2f), and significantly suppressed disease progression of Fg in germinated wheat seeds (Fig. 2g and Extended Data Fig. 3b). Moreover, during three consecutive years of field trials, ZJU23 consistently showed a clear biocontrol efficacy of 50–70% against FHB (Fig. 2h). In addition, ZJU23 substantially suppressed DON production by 50–80% during field trials (Fig. 2i). Together, these results indicate that ZJU23 is an effective biocontrol agent for the control of FHB and can be used to reduce DON contamination.

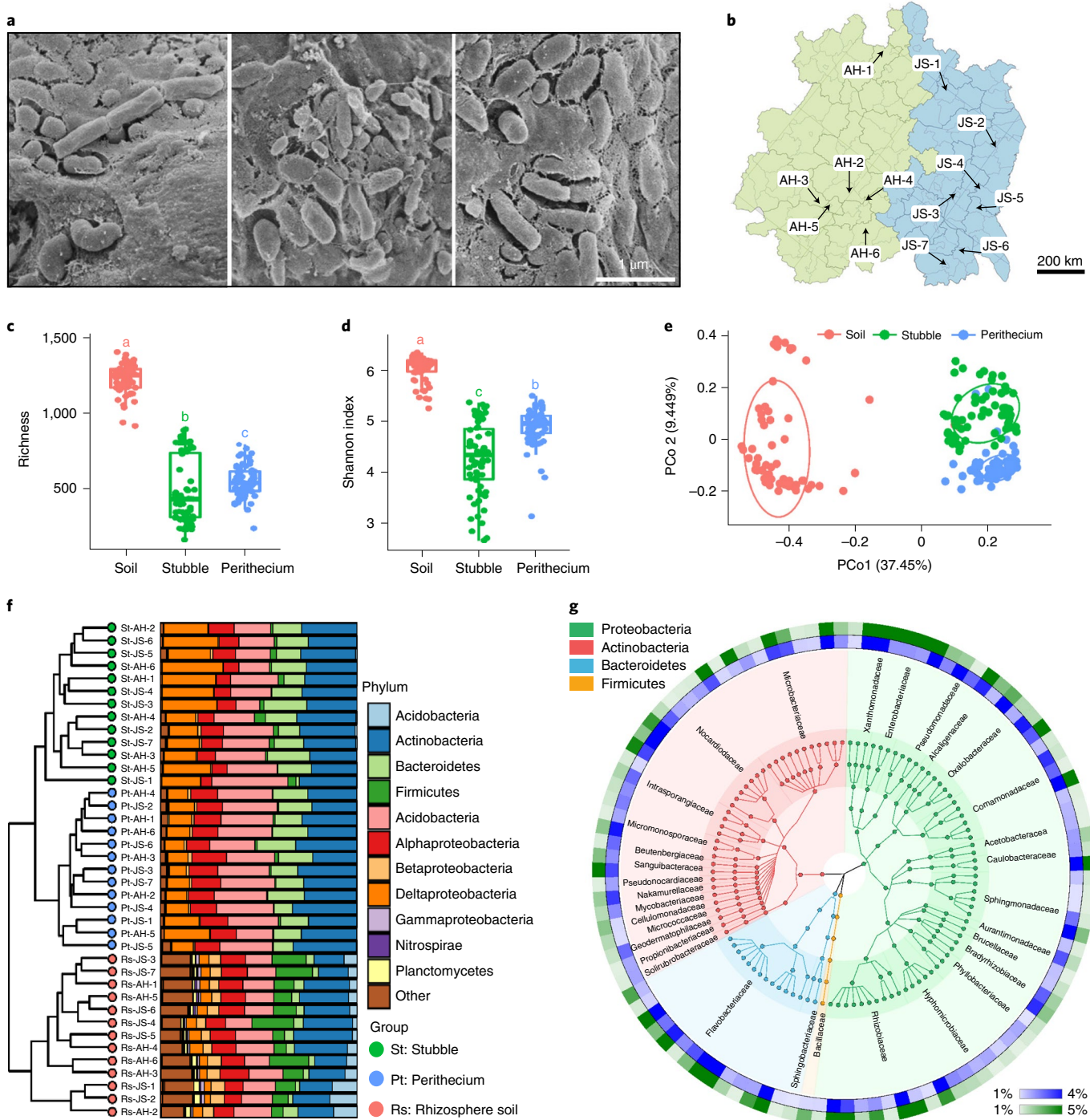


**Fig. 1 | Assessment of perithecium-associated bacterial communities.** **a**, Scanning electron microscopy observation of bacteria on perithecia collected from the field. The experiment was repeated three times with similar results. **b**, Locations of 13 sampling sites located in two Chinese provinces. AH, Anhui Province; JS, Jiangsu Province. **c-d**, Richness (**c**) and Shannon (**d**) index of the bacterial communities from perithecia, rice stubbles and soil. Different letters indicate significantly different groups ( $P < 0.001$ , ANOVA, Tukey's HSD). The horizontal lines within boxes represent medians. The tops and bottoms of boxes represent the 75th and 25th percentiles, respectively. The upper and lower whiskers extend to data no more than 1.5x the interquartile range from the upper edge and lower edge of the box, respectively. **e**, Principal coordinates analysis based on Bray-Curtis distance showing that the microbiota of perithecia is distinct from that of soil and rice stubbles ( $P = 0.001$ , PERMANOVA with ADONIS test). **f**, Stacked bar plot combined with Bray-Curtis distance-based dendrogram showing the averaged bacterial community composition for each compartment at each sampling site. The stacked bar plot includes the phylum and proteobacterial class levels as indicated. **g**, The core microbiome of perithecium-associated bacteria. The inner ring represents the OTUs that were reproducibly detected in the perithecia and infected rice stubbles with relative abundance greater than 0.1%. The relative abundances of distinct perithecium and stubble OTUs are shown as blue (perithecium) and green (stubble) heatmaps. Replicates for each compartment,  $n = 65$  biologically independent samples.

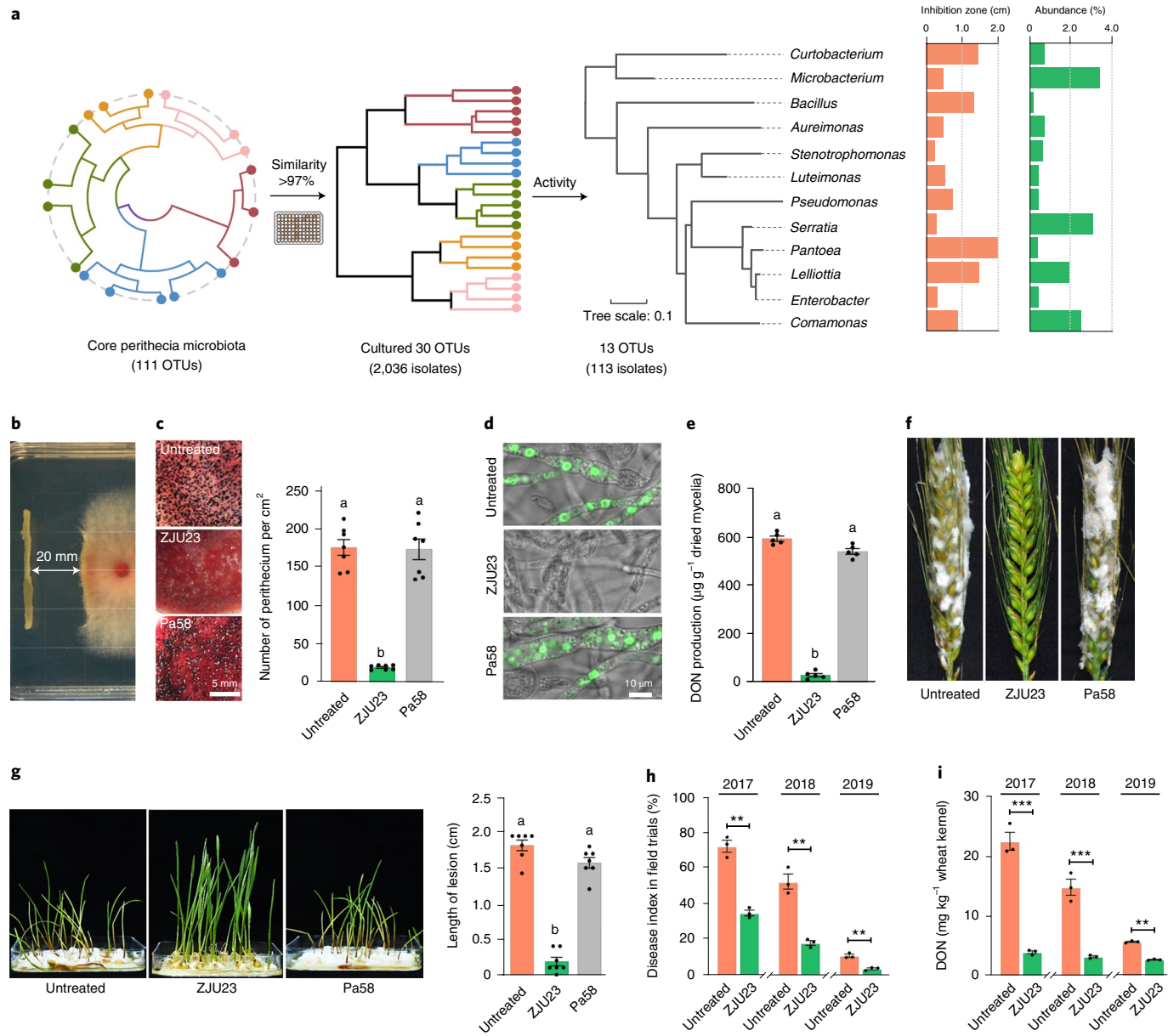


**Fig. 2 | Isolation and identification of the *F. graminearum* antagonist ZJU23.** **a**, Information of core peritheciun microbiome and cultivable bacteria recovered from *Fg* perithecia. The maximum-likelihood phylogenetic tree of the bacterial genera tree was constructed on the basis of full-length 16S rDNA sequences. The inhibition zones of representative strains and the relative abundance of corresponding OTUs in the peritheciun microbiome are included in the bar plots on the right. **b**, The antagonistic activity of ZJU23 against *Fg* PH-1. **c**, Inhibition efficiency of ZJU23 against the formation of *Fg* perithecia on carrot agar medium (left panel) and corresponding peritheciun numbers in each treatment (right panel). Data are presented as mean  $\pm$  s.e.m. of  $n=7$  biologically independent samples. Different letters indicate significantly different groups ( $P<0.05$ , ANOVA, Tukey's HSD). The non-antagonistic *P. agglomerans* Pa58 was used as a control. **d,e**, Inhibition efficiency (e) of ZJU23 against deoxynivalenol (DON) toxicosome formation and DON production. DON-toxicosome formation labelled with Trl-GFP in each treatment was observed at 60 h under toxin-inductive conditions using a confocal microscope (d). The DON production in each treatment was quantified at 7 days post-inoculation (dpi). Data are presented as mean  $\pm$  s.e.m. of  $n=5$  biologically independent samples. Different letters indicate significantly different groups ( $P<0.05$ , ANOVA, Tukey's HSD). The experiment was repeated three times with similar results (e). **f,g**, Biocontrol efficacy of ZJU23 against FHB on wheat anthers and seedlings in a growth chamber (f). The representative infected anthers are shown at 5 dpi. The lengths of lesions on wheat coleoptiles (g, right) were measured and statistically analysed ( $n=7$  biologically independent wheat coleoptiles, mean  $\pm$  s.e.m.,  $P<0.05$ , ANOVA Tukey's HSD). The experiment was repeated three times (g, left) with similar results. **h,i**, The disease index of FHB after treatment with ZJU23 (h) and efficiencies of ZJU23 in controlling DON production (i) in field trials conducted in three continuous years from 2017 to 2019. Water was used for the untreated control. Data are presented as mean  $\pm$  s.e.m. of  $n=3$  biologically independent samples, \*\*\* $P<0.001$ , \*\* $P<0.005$ , two-sided Student's t-test with false discovery rates (FDR) correction.

**HA is the antifungal compound produced by ZJU23.** To identify antifungal compound(s) produced by ZJU23 and their biosynthetic gene cluster(s), we first performed a mutagenesis screen for the loss of antifungal activity. More than 12,000 himar1

mariner transposon mutants were assessed for antifungal activity, and 80 inactive transposon mutants were identified and subsequently subjected to whole-genome re-sequencing for mapping of the insertion sites. Transposon insertions were mainly distributed

in the open reading frames of ORF3911, ORF3913 and ORF3914 and in their neighbouring ORFs (in 41 mutants) (Fig. 3a). These genes are located in a ~42 kbp DNA region in one orientation that is located on plasmid 1 as illustrated in Fig. 3b, indicating that this region is a potential biosynthetic gene cluster for the antifungal compound in ZJU23. Ten putative proteins were predicted for this gene cluster and assigned Antifungal compound biosynthetic protein A (AcbA) to AcbJ. To validate whether the AcbA–AcbJ cluster is responsible for antifungal compound biosynthesis, we constructed individual gene mutants and tested their antifungal activity. Bacterial growth was not altered in any of the mutants, when compared with ZJU23 (Supplementary Fig. 3). Eight of the mutants (that is, all mutants except those lacking ACBG and ACBJ) showed no inhibition activity towards Fg (Fig. 3c), suggesting that the AcbA–AcbJ cluster is responsible for antifungal compound biosynthesis in ZJU23.

To identify the antifungal compound synthesized by the AcbA–AcbJ cluster, we compared the metabolic profiles of ZJU23 and four deletion mutants ( $\Delta$ AcbA,  $\Delta$ AcbC,  $\Delta$ AcbD and  $\Delta$ AcbH) in the AcbA–AcbJ cluster. Unique peaks in ZJU23 identified using liquid chromatography–mass spectrometry (LC–MS) analysis are expected to correspond to peaks of antifungal compounds (Anti-Cs). Two unique peaks (Anti-C1 and Anti-C2) were specifically found in the supernatant of ZJU23, which were further purified and tested for antifungal activity (Extended Data Fig. 4a). Anti-C1 with (+)-high resolution mass spectroscopy (HR-MS) (obs.  $[M+H]^+$  at a mass-to-charge ratio ( $m/z$ )1300.7378) (Extended Data Fig. 4b) showed higher antifungal activity than Anti-C2. Analysis of 1D ( $^1$ H,  $^{13}$ C)/2D (COSY, HSQC, HMBC) NMR spectra revealed that Anti-C1 is a glycosylated lipopeptide containing nine amino acid residues. Further analysis of NOESY correlations (Supplementary Data 5 and Extended Data Fig. 4c–g) and absolute configurations of amino acids in the macrocycle peptide skeleton using Marfey's method<sup>32</sup> suggested that Anti-C1 is identical to the known lipopeptide compound HA<sup>16,17</sup> (Fig. 3d and Extended Data Fig. 5). Anti-C2 also possessed antifungal activity and was further identified as herbicin B, a deglycosylated intermediate during HA biosynthesis. Herbicin B is transformed to HA by a glycosyltransferase encoded by AcbI (Extended Data Fig. 6). In addition, LC–MS analysis further confirmed that mutants lacking either AcbA to AcbF, AcbH or AcbJ did not produce HA (Fig. 3e). HA efficiently inhibited mycelial growth in both agar plates and liquid media, and suppressed peritheciun formation, conidial germination, DON-toxisome formation and DON production (Fig. 3f–j and Extended Data Fig. 7). HA itself has antifungal activity and is not metabolized inside the cell, as indicated by comparing the metabolic profiles of HA-treated protoplast samples with those of the non-treated control using LC–MS (Supplementary Fig. 4). Taken together, HA is the major antifungal compound produced by ZJU23, and the AcbA–AcbJ cluster is responsible for HA production.

**Fig. 3 | Herbicin A is the major antifungal compound produced by ZJU23.** **a**, Distribution and frequency of transposon disrupted genes in the ZJU23 transposon mutants that lost antifungal activity. Blue dots indicate a potential active compound biosynthetic gene cluster. **b**, Potential active compound biosynthetic gene cluster and putative assignments of encoded proteins. **c**, Antifungal activity of individual deletion mutants in the biosynthetic gene cluster. Representative photographs of antifungal activity of ZJU23 or mutants against FG are shown. **d**, Structure of HA. **e**, Extracted ion chromatographic (EIC) comparison of HA production by ZJU23 and the indicated mutants. Pure HA was used as a positive control. The calculated mass of HA ( $[M+H]^+$  at  $m/z$  1300.7378) is indicated by a dashed line. **f**, Relative growth rate of Fg mycelia grown in liquid medium supplemented with the concentrations of HA indicated on the x axis was calculated from  $n=6$  biologically independent samples (mean  $\pm$  s.e.m.). The dashed line indicates the  $EC_{50}$  concentration. The experiment was repeated three times with similar results. **g**, Inhibition efficiency of HA ( $2\ \mu\text{g ml}^{-1}$ ) against the formation of Fg perithecia on carrot agar medium. The experiment was repeated three times with similar results. **h**, Inhibition efficiency of HA ( $2\ \mu\text{g ml}^{-1}$ ) against conidial germination of Fg. **i,j**, Inhibition efficiency of HA ( $8\ \mu\text{g ml}^{-1}$ ) against DON-toxisome formation and DON production. DON-toxisome formation labeled with Trl1-GFP in each treatment was observed at 36 h under toxin-inductive conditions using a confocal microscope (**i**). The DON production in each treatment was quantified at 7 dpi from  $n=5$  biologically independent samples (mean  $\pm$  s.e.m., \*\*\* $P = 9.28 \times 10^{-7}$ , two-sided Student's *t*-test) (**j**). The experiment was repeated three times with similar results (**j**). **k**, Proposed biosynthetic pathway of HA.

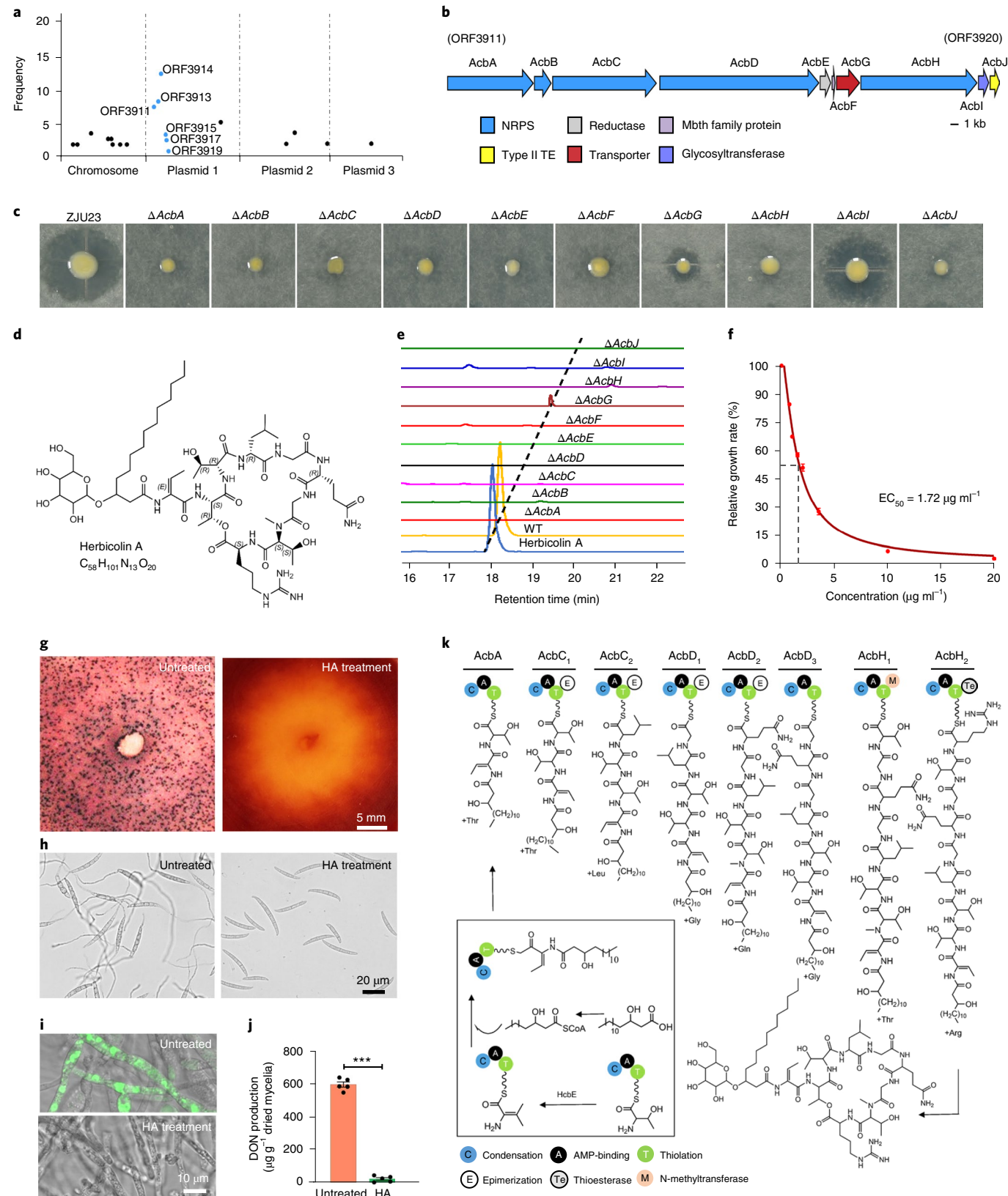
**Biosynthesis of HA and origin of AcbA–AcbJ cluster.** Subsequently, we investigated the biosynthesis process of HA by the AcbA–AcbJ cluster. AcbA, AcbC, AcbD and AcbH are non-ribosomal peptide synthetase (NRPS) proteins. A total of nine modules in these NRPSs are responsible for the activation and incorporation of nine amino acids into the growing peptide chain. In addition, the AcbH<sub>2</sub> module catalyses the cyclization by forming an ester bond between amino acids incorporated by modules AcbA and AcbH<sub>2</sub> (Fig. 3k). We performed LC–MS analyses of both the wild-type (WT) and mutant samples to detect HA and its predicted intermediates. As predicted, the different intermediates were detectable and highly accumulated in the mutants, compared with the LC–MS profile of the WT (Extended Data Fig. 4a). Furthermore, the molecular weight of emerged intermediates in each NRPS mutant was matched to the predicted intermediates (Extended Data Fig. 6). None of the identified intermediates were glycosylated, which indicated that the glycosylation modification by AcbI was the last step of HA biosynthesis. Taken together, HA is likely the product of the following biochemical pathway: AcbA to AcbC to AcbD to AcbH to AcbI (Fig. 3k).

We next traced the origin of the AcbA–AcbJ cluster. The HA biosynthetic gene cluster was either absent or discontinuous with low identity in 102 *P. agglomerans* genomes available in public databases and the control strain Pa58 (Extended Data Fig. 8a, and Supplementary Fig. 5 and Data 6). Further investigation of homologous sequences revealed that homologues of HA biosynthetic proteins were mainly retrieved from strains belonging to *Candidatus Fukatsuia symbiotica*, *Chromobacterium* spp. and *Burkholderia* spp., with high amino acid sequence identities (>40%) (Extended Data Fig. 8a,b and Supplementary Fig. 6). In addition, we noted that homologues in *Ca. F. symbiotica* had a ~38 kb cluster in a plasmid with 60% amino acid identity to the HA cluster in *P. agglomerans* (Extended Data Fig. 8c). This high level of identity was surprising because the two bacteria belong to two distinct taxonomic families (Extended Data Fig. 8d). This remarkable conservation in microsynteny and sequence homologies between ZJU23 and *Ca. F. symbiotica* gene clusters, not present in other tested *P. agglomerans* strains, raised the possibility that the HA cluster in ZJU23 was likely acquired from *Ca. F. symbiotica* via horizontal gene transfer (HGT) or underwent massive losses independently from the common ancestor of *P. agglomerans* and *Ca. F. symbiotica*.

**Fungal ergosterol biosynthesis is involved in HA resistance.** One strategy to identify drug targets is to isolate and analyse drug-resistant mutants. Given that HA also has strong inhibition activity towards *Saccharomyces cerevisiae* BY4741 ( $EC_{50} = 0.3\ \mu\text{g ml}^{-1}$ ), we isolated HA-resistant mutants in the BY4741 background on rich medium supplemented with  $6\ \mu\text{g ml}^{-1}$  HA. A total of 49 HA-resistant mutants were recovered and subsequently subjected to whole-genome sequencing to map the mutated sites. Each of the resistant mutants had at least one non-synonymous mutation, and 72 mutated sites

in 55 genes were identified (Fig. 4a and Supplementary Data 7). Notably, 9 genes were found to be directly involved in ergosterol biosynthesis (Fig. 4a). Gene Ontology (GO) analysis of the genes identified in HA resistance mutants showed a significant enrichment of sterol/ergosterol biosynthetic processes (Fig. 4b). We further tested

the HA susceptibility of available deletion mutants ( $\Delta$ Erg4,  $\Delta$ Erg6,  $\Delta$ Erg8 and  $\Delta$ Erg10) in the ergosterol biosynthetic pathway of *S. cerevisiae*, and validated that mutation of genes involved in yeast ergosterol biosynthesis conferred HA resistance. Furthermore, we examined whether ergosterol biosynthesis is also involved in HA



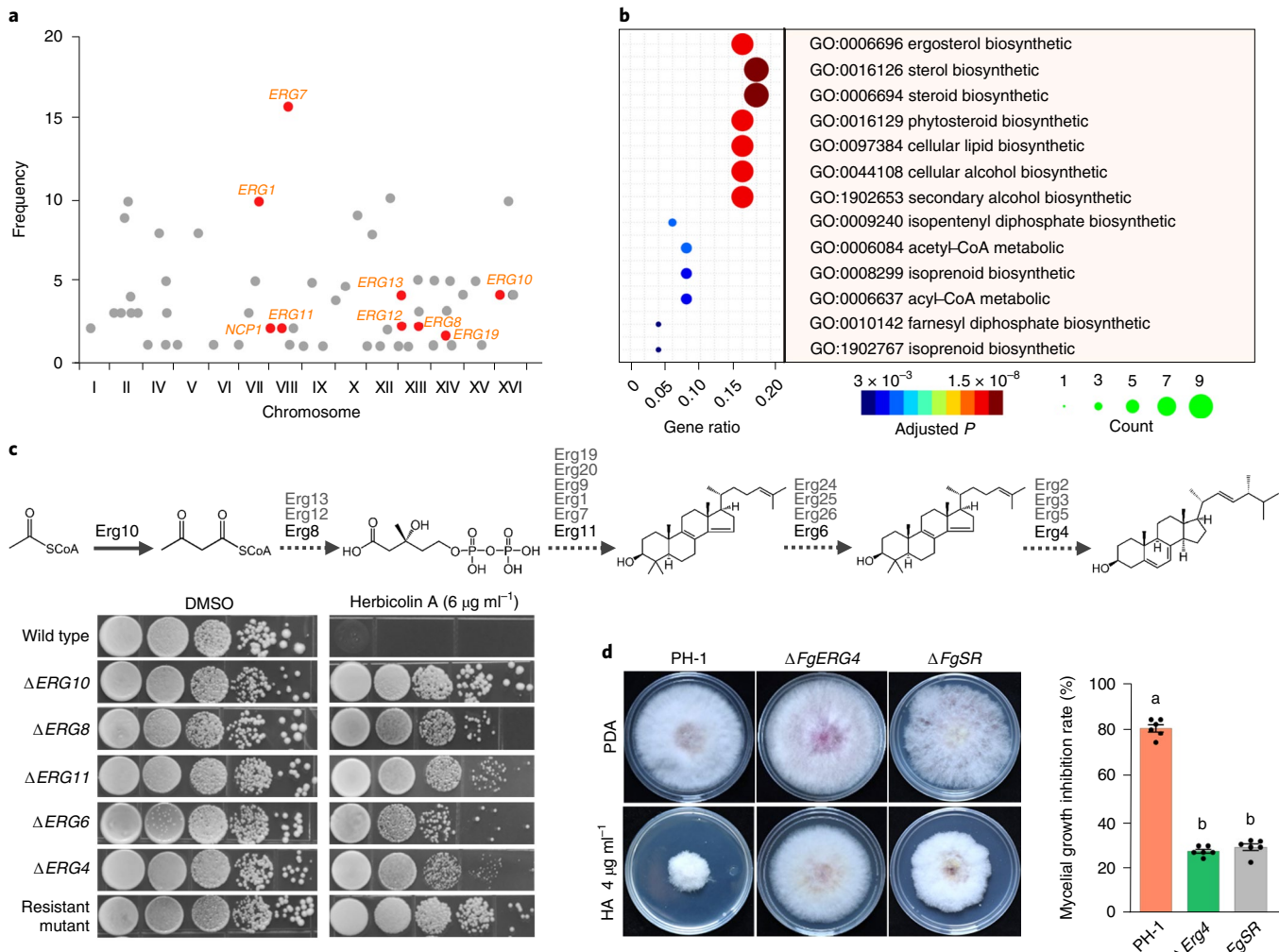


**Fig. 4 | Ergosterol biosynthesis is involved in the fungal susceptibility to HA.** **a**, The frequency of mutated genes identified by whole-genome sequencing of 49 HA-resistant mutants. Red dots represent the genes involved in ergosterol biosynthesis. **b**, GO enrichment analysis of mutated genes in **a**. The colour and size of the bubble represent the adjusted *P* value and number of enriched genes in each GO pathway, respectively. **c**, The susceptibility of ergosterol biosynthesis mutants of *S. cerevisiae* BY4741 towards HA at  $6 \mu\text{g ml}^{-1}$ . One HA-resistant mutant in **a** was used as a control (bottom). Schematic diagram of the ergosterol biosynthetic pathway in fungi. Critical ergosterol biosynthetic enzymes are shown. Broken arrows, multiple enzymatic steps; solid arrows, single enzymatic step (top). **d**, Left: the susceptibility of ergosterol biosynthesis mutants  $\Delta FgErg4$  and  $\Delta FgSR$  in *Fg* towards HA at  $4 \mu\text{g ml}^{-1}$ . Right: mycelial growth inhibition of HA against the wild type,  $\Delta FgErg4$  and  $\Delta FgSR$  of *Fg* was calculated from  $n=6$  biologically independent samples (mean  $\pm$  s.e.m.). Different letters indicate significantly different groups ( $P < 0.05$ , ANOVA, Tukey's HSD). The experiment was repeated three times with similar results. PDA stands for Potato Dextrose Agar.

resistance in *Fg*. *FgErg4* and *FgSR* are critical for ergosterol production and virulence for *Fg*<sup>33,34</sup>. Susceptibility tests indicated that mutants lacking each of these proteins had significantly increased HA resistance (Fig. 4d), similar to that observed in *S. cerevisiae* (Fig. 4c). Together, these data suggest that the ergosterol biosynthetic process is involved in the fungal susceptibility to HA.

**HA interacts with ergosterol and disrupts fungal lipid rafts.** The fungal cell lipid plasma membrane naturally contains regions rich in ergosterol and sphingolipids<sup>35</sup>. As the antifungal activity of HA seemed to be connected with ergosterol (Fig. 4), we wondered whether HA directly interacts with ergosterol-containing plasma membranes. To elucidate this, *Fg* protoplasm was incubated with HA, and the plasma membrane was subsequently extracted. An LC-MS assay was used to quantify HA in the fractionated samples. HA was more abundant in the plasma membrane fraction than in the cytosolic fraction and in the supernatant collected through centrifugation after the incubation (Fig. 5a). To further identify which

fungal plasma membrane component is necessary for the retention of HA, major components of the fungal plasma membrane, including ergosterol, sphingomyelin (SM), phosphatidylethanolamine (PE), 1,2-dipalmitoyl-sn-glycero-3-phosphocholine (DPPC) and 1,2-dioleoyl-sn-glycero-3-phosphocholine (DOPC) were individually coated onto glass discs and air-dried. Subsequently, they were covered with an HA solution. Results indicated that HA was mainly retained by ergosterol in this assay (Fig. 5b).

As HA interacts with ergosterol and associates with ergosterol-enriched cell membranes, we wondered whether HA affects the integrity of lipid rafts in *Fg*. We first observed the influence of HA on the morphology of artificial lipid rafts using atomic force microscopy (AFM). Although these artificial lipid rafts on a mica support are distinct from those on a real biological membrane, our previous study suggested that the components of the artificial lipid rafts behave similarly to those of biological membranes<sup>36</sup>. HA drastically changed the appearance of reconstituted lipid rafts containing ergosterol, with a clear dissolution of the elevated plains

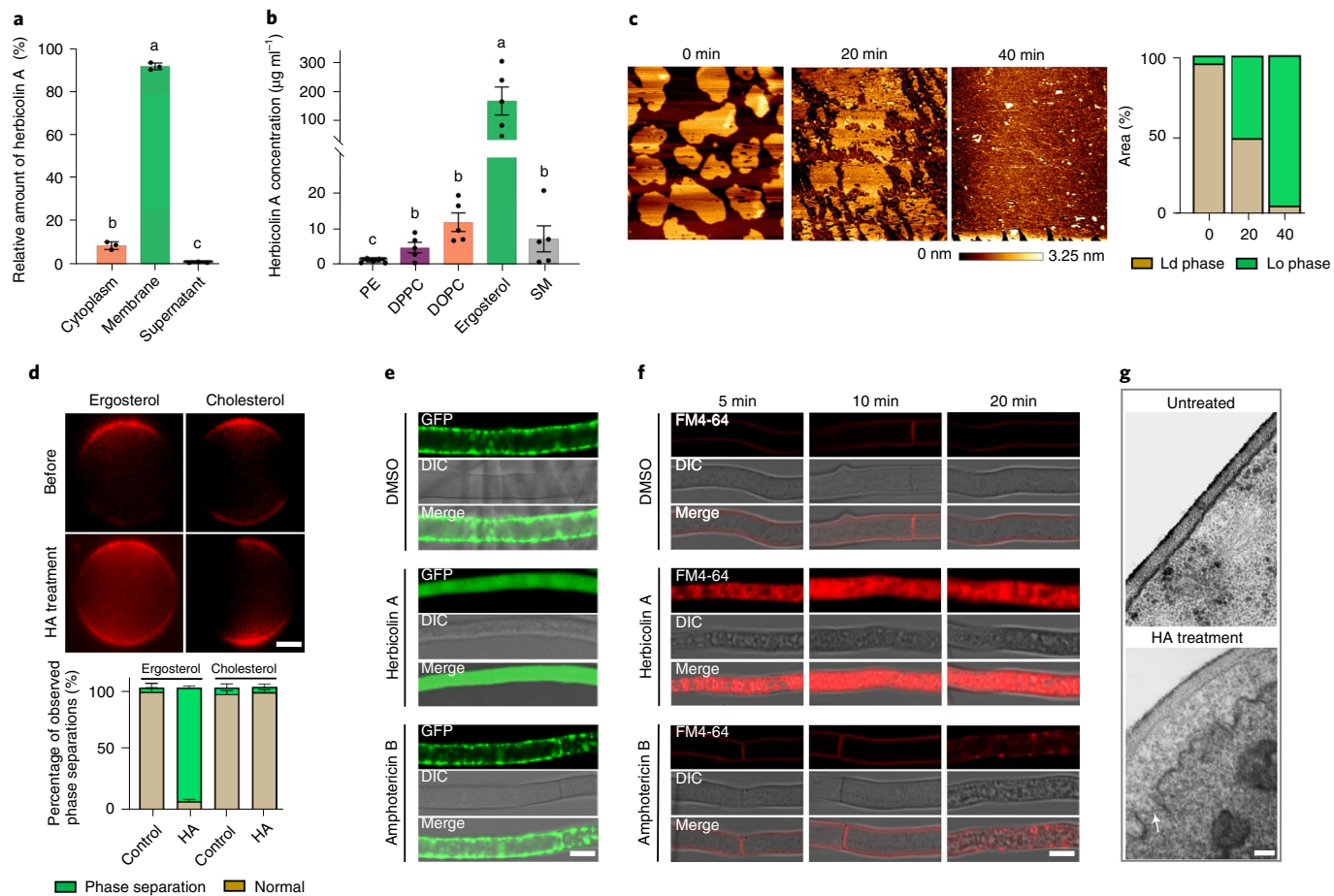


**Fig. 5 | HA interacts with ergosterol and targets fungal lipid rafts.** **a**, Distribution of HA in Fg protoplasts. The relative amount of HA in each fraction was calculated from  $n=3$  biologically independent samples (mean  $\pm$  s.e.m.). Different letters indicate significantly different groups ( $P < 0.05$ , ANOVA, Tukey's HSD). **b**, HA retention capability of various lipids. The retained HA was quantified by LC-MS from  $n=5$  biologically independent samples (mean  $\pm$  s.e.m.). Different letters indicate significantly different groups ( $P < 0.05$ , ANOVA, Tukey's HSD). **c**, Effect of HA on artificial lipid rafts. The atomic force microscopy elevation maps (left) and statistical results of the percentage of the elevated phases (right) within the ordered lipid domains at different timepoints are shown. **d**, Effect of HA on lipid domains of giant unilamellar vesicles (GUVs). GUV containing ergosterol or cholesterol, spiked with 0.1% lipid-conjugated fluorescent dye, were treated with 10  $\mu\text{M}$  HA or left untreated. Top: representative original images from hundreds of GUVs analysed. Scale bar, 8  $\mu\text{m}$ . Bottom: statistical analysis of different types of GUVs from 100 GUVs of  $n=3$  biologically independent samples (mean  $\pm$  s.e.m.). Brown, normal GUV; Green, dissolution of GUV. **e**, Localization of the lipid raft marker FgStoA-GFP in various treatments. The final concentration of HA and amphotericin B was 5 and 8  $\mu\text{g ml}^{-1}$ , respectively (EC<sub>90</sub> of HA or amphotericin B). The solvent DMSO was used as a control. Scale bar, 5  $\mu\text{m}$ . DIC stands for differential interference contrast. **f**, Fungal membrane permeability following various treatments. Mycelia of Fg treated with HA (6.5  $\mu\text{M}$ ) or amphotericin B (6.5  $\mu\text{M}$ ) were stained with FM4-64 dye and observed at the indicated timepoints after treatment. Scale bar, 5  $\mu\text{m}$ . **g**, Transmission electron micrographs of plasma membrane changes caused by HA treatments in Fg. Scale bar, 0.1  $\mu\text{m}$ . The white arrow indicates a pole. All experiments were repeated three times with similar results.

(Fig. 5c). Furthermore, we created giant unilamellar vesicles (GUVs) of defined lipid compositions with fluorescent DiD (1,1-Dioctadecyl-3,3,3,3-tetramethylindodicarbocyanine) labelling the lipid disorder phase<sup>37</sup>. Upon HA treatment, the phase partitioning of fluorescent DiD in GUVs was rapidly shifted because of phase separation, revealing a dissolution effect (Fig. 5d). However, phase separation was not observed after HA addition in the GUVs containing cholesterol (Fig. 5d), indicating that HA specifically disrupted the ergosterol-containing artificial lipid raft.

Stomatin protein StoA has been identified as a marker for fungal lipid rafts<sup>38</sup>. We next constructed an Fg strain expressing the StoA orthologue FgStoA-GFP (encoded by FGSG\_10909) to indicate Fg lipid rafts, and determined the effect of HA on lipid rafts in vivo. In the solvent or the fungicide amphotericin B treatment, FgStoA-GFP mainly localized along the plasma membrane of mycelia and protoplasm (Fig. 5e). However, upon HA treatment, the plasma membrane

localization of FgStoA-GFP was dramatically diminished, and the fused protein was mainly diffused in the cytoplasm (Fig. 5e). Furthermore, HA treatment resulted in increased membrane permeability indicated by plasma membrane dye FM4-64 staining (Fig. 5f). Subsequently, transmission electron microscopy observations indicated that the architecture of cell plasma membranes, but not cell wall, was markedly changed (Fig. 5g and Supplementary Fig. 7). In addition, the in silico modelling approach showed that the acyl chain of HA rapidly penetrated the bilayer and was only stable when ergosterol was present in the lipid membranes (Supplementary Fig. 8, and Videos 1 and 2). These results suggested that HA is directly inserted into the Fg plasma membrane by interacting with ergosterol. This interaction echoes observation that yeast mutants with a deficiency in ergosterol biosynthesis were resistant to HA (Fig. 4). Collectively, HA was shown to target ergosterol-containing lipid rafts and to disrupt the integrity of the cell plasma membrane in Fg.

**HA exhibits broad-spectrum antifungal activity.** As ergosterol is highly conserved in fungal plasma membranes, we decided to examine whether ZJU23 and HA are effective in antagonizing other important phytopathogenic fungi. Both ZJU23 and HA substantially inhibited the mycelial growth of all tested fungal pathogens *in vitro* (Fig. 6a,b). The half maximal effective concentration ( $EC_{50}$ ) of HA in these tested species falls in the same range as that against Fg (Fig. 3f). HA also substantially inhibited spore germination of *Botrytis cinerea* (Fig. 6c, left), and significantly reduced the severity of grey mould disease on tomato (*Solanum lycopersicum*) and strawberry (*Fragaria × ananassa*) leaves by 93% and 91%, respectively, at a final concentration of  $2\text{ }\mu\text{g ml}^{-1}$  (Fig. 6d,e). Furthermore, HA ( $5\text{ }\mu\text{g ml}^{-1}$ ) effectively suppressed the appressorium formation of *Magnaporthe oryzae* (Fig. 6c, right) and decreased the infection lesion area by 86% in barley (*Hordeum vulgare*) leaves (Fig. 6f). We then examined the impact of HA on the human opportunistic fungal pathogen *Candida albicans* and found that HA effectively inhibited the growth of *C. albicans* YW02 with  $EC_{50}=0.0368\text{ }\mu\text{M}$ , which is more efficient than the clinical fungicides amphotericin B ( $EC_{50}=0.173\text{ }\mu\text{M}$ ) and fluconazole ( $EC_{50}=5.2\text{ }\mu\text{M}$ ) (Fig. 6g). Furthermore, we found that *Aspergillus fumigatus* CBS101355 was also more susceptible to HA with  $EC_{50}=0.38\text{ }\mu\text{M}$ , compared with amphotericin B ( $EC_{50}=6.5\text{ }\mu\text{M}$ ) and fluconazole ( $EC_{50}=13\text{ }\mu\text{M}$ ) (Fig. 6h).

Next, we investigated whether HA was able to inhibit the mycelial growth of fungicide-resistant Fg strains. Four categories of resistant strains were tested, which show resistance to carbendazim, phenamcaril, fludioxonil and tebuconazole, targeting fungal tubulin, myosin I, hybrid histidine kinase and sterol 14 $\alpha$ -demethylases, respectively. All tested resistant strains were susceptible to HA, indicating that there is no cross-resistance between HA and other tested fungicides (Fig. 6i). Moreover, HA showed synergistic effects with two commonly used fungicides for plant fungal disease control, polyoxin B and carbendazim (Extended Data Fig. 9). Collectively, these results indicated that HA is a potential effective chemical against fungal diseases in both crops and animals, and might be applicable for the management of fungicide resistance issues in agriculture.

## Discussion

Like animals and plants, fungi are also associated with distinct bacterial communities. However, fungal microbiomes remain poorly understood when compared with those of other hosts<sup>12,39</sup>. In the present study, we observed that distinct bacteria are associated with the sexual fruiting bodies of *Fusarium graminearum*. Microbiome profiling revealed that perithecia from geographically distant locations harboured very similar bacterial communities. Source tracking analyses indicated that the identified bacteria were mainly acquired from adjacent rice stubbles, but with different abundance. This finding indicates that microbiota assembly of fungal fruiting bodies is already initiated during the infectious stage of the

pathogen. Previous studies have suggested that the environment and host-specific factors together determine host microbiome assembly<sup>40–44</sup>. As perithecia from different field sites showed a similar core bacterial composition, it is evident that Fg has a strong shaping effect on its microbiota. Chemical-guided communication between microbes was recently recognized as an important factor shaping communities<sup>12,39,45,46</sup>. Previous studies indicated that the Fg genome can harbour up to 67 gene clusters involved in secondary metabolism, and some of the biosynthesized compounds showed antimicrobial activity<sup>47–49</sup>. Therefore, we propose that secondary metabolic compounds of Fg perithecia play an important role in shaping the associated microbiome. Recently, distinct fungal compounds have been reported to have a strong effect on the associated bacterial communities<sup>50</sup>, supporting our hypothesis.

Our results indicated that a fungal pathogen's microbiome naturally harbours antagonists in addition to mutualistic colonizers as observed before<sup>29</sup>. Although individual bacteria can have negative impacts on the host fungus, these bacteria probably do not prevail under natural conditions. However, when biotechnologically enriched and re-applied, they may be applicable for plant protection. In this study, *P. agglomerans* ZJU23 was isolated from Fg perithecia and displayed the highest antagonistic activity towards mycelial growth of Fg. ZJU23 effectively suppressed Fg peritheciun formation, mycotoxin biosynthesis and development of Fusarium head blight at high concentrations, while naturally associated with perithecia at lower concentrations (Fig. 2a).

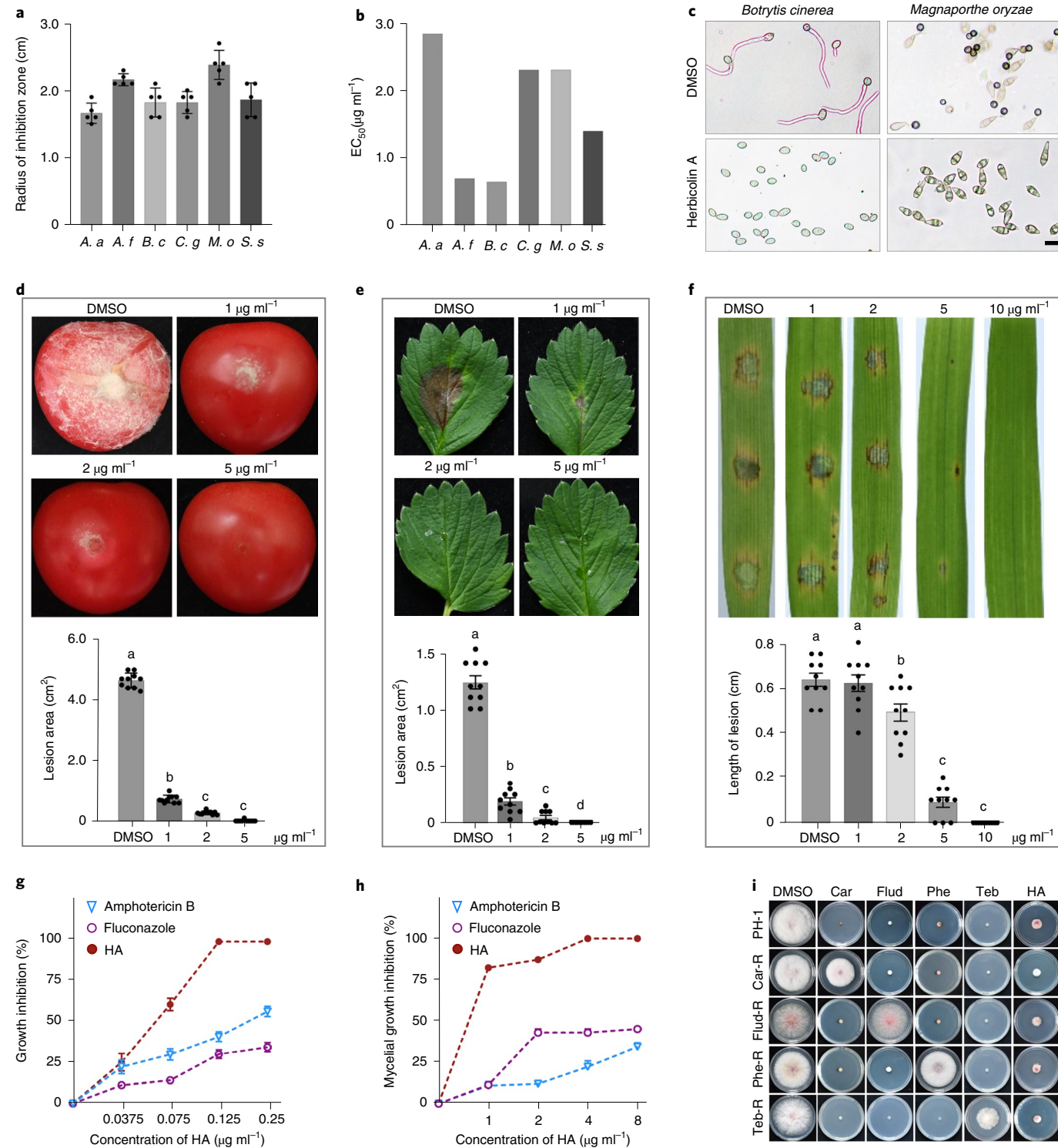
Antagonism within members of the microbiota was described before, but our general understanding of the molecular mechanisms involved in such microbial interaction is still limited<sup>51–53</sup>. Deciphering yet unknown microbial interaction mechanisms will provide the basis for the engineering of beneficial microbiomes that protect host plants and animals<sup>3,9,54</sup>. A detailed investigation of the antagonistic effects between *P. agglomerans* ZJU23 and Fg showed that HA is the involved bioactive compound. Although HA was identified around 40 years ago<sup>16–18</sup>, the biosynthetic gene cluster of HA and its mode of action (MOA) towards fungi were hitherto unknown. By combining various approaches, we showed that the AcbA-AcbJ gene cluster is responsible for HA biosynthesis in ZJU23 and unexpectedly discovered that ZJU23 most probably attained the ability to produce HA via horizontal gene transfer.

HA consists of a peptide ring with eight amino acids to which a fatty acid chain, a dehydrobutyric acid and a sugar moiety are attached<sup>55</sup>. The MOA of cyclic lipopeptides against fungi are mostly unknown<sup>56</sup>. For example, the MOA of various well-known surfactins and fengycins produced by *Bacillus* species are still not completely understood; they may interact with phosphatidylethanolamine or the cell wall, by inhibiting DNA synthesis or by interrupting the integrity of mitochondria<sup>57–60</sup>. Another MOA was observed for Iturin A and syringomycin, which inhibits fungi via a pore-dependent mechanism<sup>61</sup>. Echinocandins secreted by *Aspergillus* spp. inhibit the

**Fig. 6 | HA exhibits broad-spectrum antifungal activity.** **a**, Antagonistic activity of ZJU23 against six plant-pathogenic fungi. The radius of the inhibition zone (cm) was measured for each co-culture of ZJU23 with *Alternaria alternata* (A. a), *Aspergillus flavus* (A. f), *Botrytis cinerea* (B. c), *Colletotrichum gloeosporioides* (C. g), *Magnaporthe oryzae* (M. o) and *Sclerotinia sclerotiorum* (S. s). Data are presented as mean  $\pm$  s.e.m.,  $n=5$  biologically independent samples. The experiment was repeated three times with similar results. **b**,  $EC_{50}$  of HA against tested plant fungal pathogens. **c**, Inhibition activity of HA on spore germination of *B. cinerea* and appressorium formation of *M. oryzae*. Representative images were taken after 3 h of incubation with HA at  $5\text{ }\mu\text{g ml}^{-1}$ . Scale bar,  $10\text{ }\mu\text{m}$ .  $n=100$  spores. **d–f**, Effect of HA on diseases caused by *B. cinerea* and *M. oryzae* in planta. The inoculated *B. cinerea* (d,e) or *M. oryzae* (f) spore suspension was supplemented with the indicated concentration of HA, and then inoculated onto tomato fruit (d, top), strawberry leaves (e, top) or barley leaves (f, top). The area or length of lesions was measured (bottom) and statistically analysed from  $n=10$  biologically independent fruits or leaves (mean  $\pm$  s.e.m.). Different letters indicate significantly different groups ( $P<0.05$ , ANOVA, Tukey's HSD). DMSO was used as a solvent control. The experiment was repeated three times with similar results. **g,h**, Growth inhibition rate of HA, amphotericin B and fluconazole at various concentrations in *C. albicans* YW02 (g) and *A. fumigatus* CBS101355 (h) (mean  $\pm$  s.e.m.,  $n=3$  and 6 biologically independent samples for *C. albicans* YW02 and *A. fumigatus* CBS101355, respectively). The experiment was repeated three times with similar results. **i**, Antifungal activity of HA against fungicide-resistant Fg strains. The final concentration of the fungicides or HA was  $5\text{ }\mu\text{g ml}^{-1}$ . Images were taken after 3 d of incubation. Car, carbendazim; Flud, fludioxonil; Phe, phenamcaril; Teb, tebuconazole. Car-R, Flud-R, Phe-R and Teb-R indicate fungicide-resistant strains. The experiment was repeated three times with similar results.

synthesis of  $\beta$ -(1,3)-glucan and thus damage the fungal cell wall<sup>62</sup>. Here we found that HA interacts with ergosterol. Furthermore, we established that HA quickly disrupts the integrity of artificial membranes containing ergosterol, but not those containing cholesterol. Complementary microscopy observation showed that HA treatment disrupted lipid rafts, increased membrane permeability, resulted in the formation of abnormal cell membranes and ultimately caused cell death. Mutations in fungal ergosterol biosynthetic pathways resulted in resistance towards HA in *S. cerevisiae* and Fg. Therefore,

our data suggest that the MOA of HA is mainly through disrupting lipid rafts in cell membranes by directly interacting with ergosterol (Extended Data Fig. 10). It should be noted that the lipid tail itself is not inhibitory, since various tested compounds with differing lipid tails did not exert antifungal activity (Supplementary Fig. 9). In addition, the antifungal activity of HA and ZJU23 was eliminated when the amino acid ring structure in HA was opened by disrupting the *ACBH* gene. This suggests that the ring structure in HA is essential for its activity.



In the present study, we also characterized the Fg peritheciun-associated microbiome presumably for the first time in a large-scale approach. This approach allowed us to understand the role of commensal bacteria in the suppression of fungal disease. We determined that the biocontrol agent ZJU23 secretes HA to inhibit Fg by interacting with ergosterol-containing cell membranes. HA has a broad antifungal spectrum and control efficiency towards phytopathogenic fungi. During the past few years, antimicrobial peptides have emerged as potential candidates for developing new antifungal therapies because they are often characterized by negligible host toxicity and low resistance rates<sup>56</sup>. HA inhibited the growth of the human opportunistic pathogen *Candida albicans* more efficiently than the clinical fungicides amphotericin B and fluconazole. In addition, HA has no visible phytotoxicity towards plant tissues (Supplementary Fig. 10). An acute oral toxicity test of pure HA indicated low toxicity in mice (Supplementary Data 8). Although HA is a potential candidate for agricultural and clinical applications, further experimentation is required to develop viable application modes of either the pure compound or microbes harbouring the respective biosynthetic cluster.

## Methods

**Community profiling based on 16S rRNA gene sequencing.** The DNA for each sample was extracted with the FastDNA SPIN kit (MP Biomedicals) according to the manufacturer's instructions. The V5–V7 region of the bacterial 16S rRNA gene was amplified by degenerate PCR primers 799F and 1193R. Two consecutive PCR reactions were carried out according to previous reports<sup>60</sup>. The barcoded amplicons were sequenced on an Illumina NovaSeq6000 platform with 2 × 250 bp reads. The 16S rRNA gene sequences were analysed with EasyAmplicon v1.09<sup>44</sup>, which includes QIIME v1.9.1<sup>61</sup>, QIIME2 v2020.11<sup>66</sup> and USEARCH v11.0.667<sup>57</sup>. All sample metadata are included in Supplementary Data 1. Sequencing library splitting was conducted with the split\_libraries\_fastq.py command in QIIME. Then, the paired-end Illumina reads were processed with USEARCH as previously described<sup>63</sup>. Sequences were clustered into OTUs at 97% similarity and the representative sequences were picked with the UPARSE algorithm in USEARCH (-cluster\_otsu command)<sup>48</sup>. All OTUs were aligned to the SILVA 132<sup>69</sup> database to remove chimeric sequences with the UCHIME algorithm<sup>70</sup> in USEARCH (-uchime2\_ref command). The taxonomy of the representative sequences was classified with the 'RDP trainset 16' database<sup>71</sup> on the basis of the syntax algorithm in USEARCH (-sintax command). OTUs assigned to chloroplasts and mitochondria were removed as host contamination by using the respective script in EasyAmplicon. An OTU table was generated within USEARCH (-otutab command). For alpha and beta diversity, samples were first rarefied at minimal sequences 5,933 by USEARCH (-otutab\_norm command). Subsequent diversity analyses were carried out using EasyAmplicon and QIIME2. The core microbiome of perithecia was defined as that containing OTUs with a relative abundance greater than 0.1% in the perithecia and associated stubble microbiome. Cladograms were visualized by GraPhAn v0.9.7. Figures were visualized by using the ggplot2 v.2.3.2 package in R v4.0.3 and ImageGP<sup>2</sup> (<http://www.ehbio.com/ImageGP/>). Clustering trees were visualized by ggtree v2.2.4 in R. The Bayesian source tracking model was used for identifying the source of peritheciun-associated microbiota with Sourcetracker<sup>73</sup>. All related tables are included in Supplementary Data 2. For the reproducibility of analyses with custom scripts, all information is available at <https://github.com/YongxinLiu/WheatFHB>. Samples of each site were used for sequencing, with five technical repeats.

### Bacterial isolation, identification and assessment of antifungal activity.

Perithecia were vortexed in phosphate-buffered saline (PBS) buffer (E607016, Sangon Biotech) for 5 min and then ground with sterile mortar and pestle. Homogenized peritheciun samples were then allowed to settle for 15 min and the supernatants were serially diluted, the resulting supernatants were plated and cultivated on 9 cm Petri dishes in 1:10 (v/v) tryptic soy medium, Reasoner's 2A agar medium and Luria-Bertani (LB) medium (details in Supplementary Methods) for 3 d at 30 °C<sup>30</sup>. Antagonistic activity of bacterial isolates towards Fg PH-1 was assessed with a dual-culture assay in Waksman's agar<sup>74</sup>. All isolates were tested in triplicates, and their inhibition zones were measured after 3 d of dual-culture cultivation at 25 °C. The genome of ZJU23 was sequenced using the PacBio RSII sequencing platform. ZJU23 and the 13 other representatives of *Pantoea* spp. with complete genome sequences were selected to construct a phylogenetic tree with ten housekeeping genes 16Sr DNA, *aroE*, *dnaA*, *guA*, *gyrB*, *mutL*, *ppsA*, *pyrC*, *recA* and *rpoB* using the neighbour-joining method with Molecular Evolutionary Genetics Analysis version 4.0.

**Production, purification and characterization of HA.** To identify antifungal compounds, ZJU23 or its mutants were grown in King's B medium for 3 d at 30 °C, before bacterial cells were removed by centrifugation. The fermentation medium

was extracted with Diaion HP-20 resin (13605, Sigma-Aldrich) and then eluted with methanol to obtain crude extracts with an evaporator. The crude sample was dissolved in a methanol solution and then subjected to purification with preparative high performance liquid chromatography (HPLC; C18 column, 5 m, 100.0 mm × 21.2 mm; 10 ml min<sup>-1</sup>, 20–100% MeOH/H<sub>2</sub>O in 30 min, followed by 100% MeOH in 10 min) to produce sub-fractions. The unique peaks in the ZJU23 sub-fraction showing antifungal activity were subjected to a semipreparative HPLC (C18 column, 5 m; 250.0 mm × 10.0 mm; 3 ml min<sup>-1</sup>; with 0.1% formic acid in 54% MeOH/H<sub>2</sub>O in 53 min, 65% MeOH/H<sub>2</sub>O in 53 min–70 min) to obtain pure compound. NMR spectra were recorded in methanol-d<sub>4</sub> on Bruker AVANCE II 400 MHz; high-resolution mass spectra were obtained on an Agilent 6530 Accurate-Mass Q-TOF LC/MS coupled to an Agilent 1260 HPLC.

**Isolation of HA-resistant yeast mutants and whole-genome sequencing.** To select for HA resistance, overnight cultures of a wild-type *S. cerevisiae* (BY4741) strain were grown in YEPD at 30 °C. Cells were plated on YEPD containing HA (6 µg ml<sup>-1</sup>). Experiments were performed in 10 biological replicates; plates were incubated at 30 °C for 5 d. The whole genomes of mutants and the wild-type strain were sequenced using an Illumina NovaSeq PE150 instrument at Beijing Novogene Bioinformatics Technology. Single nucleotide polymorphism, insertions and deletions (indel), as well as structural variations, were searched with genomic alignments.

### Construction of transposon mutants and gene deletion mutants in ZJU23.

Transposon mutagenesis was conducted to screen mutants without antagonistic activity<sup>75</sup>. The donor *Escherichia coli* SM10<sub>λ</sub>pir carrying plasmid pSC123, and the recipient *P. agglomerans* ZJU23 which was induced to be resistant to rifampicin, were grown in LB medium supplemented with kanamycin and rifampicin overnight, respectively. The supernatant was removed by centrifugation at 5,000 × g, and the pellets were washed with fresh LB medium twice and resuspended in 100 µl medium. The strains were combined and spotted in 100 µl volumes on 0.45 µm millipore filter (F513132, Sangon Biotech) on antibiotic-free LB-agar and incubated overnight at 30 °C. Then the filters were removed, the cells were vortexed in 1 ml LB, diluted and plated onto LB plates containing 50 µg ml<sup>-1</sup> kanamycin and 50 µg ml<sup>-1</sup> rifampicin. The Petri dishes were incubated at 30 °C for 3 d or until visible colonies developed. The whole genomes of the transformants were sequenced and analysed by Beijing Novogene Bioinformatics Technology. For generation of gene deletion mutants of ZJU23, a PCR-based, λ phage recombinase method was used for targeted deletions. The coding region of the target genes was replaced with the selection marker, conferring resistance to kanamycin. All transformations, selections and confirmations of mutants were conducted using the λ phage recombinase as previously described<sup>76</sup> (Supplementary Methods). Primers used for gene deletions are listed in Supplementary Data 9.

**HA molecule retention and lipid-binding assay.** The HA molecule retention assay was performed as described in a previous study<sup>36</sup>. To perform the membrane retention assay, protoplasts of Fg were incubated with homoserine lactones (HSLs) at 30 °C. Then, the cells and supernatants were collected separately by centrifugation (194 × g for 5 min). The protoplasts were treated with buffer 1 (20 mM Tris-HCl, 2 mM EDTA, 1 mM dithiothreitol and 10% glycerol) on ice to break the membrane. Cytosol and membrane fragments were separated by ultracentrifugation (179,000 × g for 24 min at 4 °C). The membrane fragments were dissolved in buffer 2 (buffer 1 with 1% Triton X-100). HA in the fractions was dried by rotary evaporation and resolved with methanol in equivalent volumes and subsequently analysed using the Agilent 6460 LC system (Agilent Technologies). The relative amount of HA was calculated from three technical replicates. The experiment was repeated three times with similar results.

The binding ability of HA to various lipids was analysed using the lipid-binding assay<sup>36</sup>. One mg per ml of each lipid species in chloroform was coated on round glass slides by evaporation. Then, the glass slides were incubated with 10 µM HA in dimethyl sulfoxide (DMSO) with PBS at 37 °C. After the incubation, the glass slides were carefully washed with PBS 4–5 times and the lipids were dissolved in DMSO. The amount of HA in each sample was measured by LC-MS. eSM (860061), DOPC (850375), DPPC (850355) (Avanti Polar Lipids) and ergosterol (45480, Sigma-Aldrich) were used. The relative amount of HA was calculated from five technical replicates. The experiment was repeated three times with similar results.

**Microscopy imaging.** Green fluorescence signalling of Tri1-GFP-labelled Fg and red fluorescence signalling of FM4-64 were visualized using a Zeiss LSM780 confocal microscope (Carl Zeiss). The survival assay of fungi was performed as previously described with modifications<sup>77</sup>. In brief, after inoculation of *F. graminearum*\_StoA-GFP for 48 h in YEPD liquid medium, various concentrations of HA were added and the mixture was incubated for up to 2 h. Subsequently, 0.2 µl of Live/Dead solution from the Fixable Red Dead cell stain kit (Thermo Fisher) was added to 100 µl of YEPD liquid medium with the *F. graminearum*\_StoA-GFP, followed by incubation for 5 min on a rotator at r.t. The stained mycelia were placed onto microscopic slides and analysed by fluorescence microscopy using the 488 nm and 561 nm lasers. Transmission electron microscopy for visualization of fungal cell membranes was employed as

previously described<sup>77</sup> using a Hitachi H7650 transmission electron microscope, operated at 80 Kv (details in Supplementary Methods). The experiment was repeated three times with similar results.

**Preparation of giant unilamellar vesicles and permeability analyses.** Chloroform solutions of lipid mixtures (DOPC/eSM/ergosterol, 2/2/1) doped with 0.5% lipid-conjugated fluorescent dye (V22887, Invitrogen) were placed onto a clean indium tin oxide (ITO)-coated glass surface within an area delimited by a rectangular silicone gasket, and the solvent was then removed under vacuum. Sucrose solution (0.1 mol l<sup>-1</sup>) was carefully added to the chamber at the edge of the gasket. The filled chamber was then sealed with another ITO-coated glass and then transferred into an oven at a temperature that was 80 °C above the highest melting temperature of any of the lipids present. At the same time, a 1.4 V<sub>p-p</sub> (peak to peak) and 10 Hz sine-wave voltage was applied on the ITO-coated glasses for 60–90 min as previously described<sup>78,79</sup>. For lipid domain rearrangement experiments, an analogue of DiIC18 (1,1'-dioctadecyl-3,3',3'-tetramethylindocarbocyanine perchlorate) with extended conjugation, DiD-C18, was excluded from the lipid order phase (Lo) into the lipid disorder phase (Ld) for GUVs<sup>37</sup>, which were used to characterize the Ld phase lipid domain. The rearrangements before and after the 10 μM HA treatment for 20 min were recorded under a total internal reflection fluorescence microscope (FV1200, Olympus). The experiment was repeated three times with similar results.

**AFM.** A chloroform solution of the lipids (DOPC/ergosterol/eSM, 3/1/6) was mixed in glass vials and dried under vacuum to remove the solvent. After resuspending the dried lipid in 10 mM HEPES buffer (including 150 mM NaCl), tip-sonication was employed to generate a clear solution, enabling the creation of nanosized tiny unilamellar vesicles. In a fluid cell, the vesicle solution (150 μl) was introduced to cleaved mica attached to a glass substrate. The vesicle sample was incubated at 37 °C for 2 min and then at 65 °C for 15 min, followed by rinsing with HEPES buffer (with 150 mM NaCl) at 65 °C to remove excess vesicles. Images were acquired with AFM at room temperature on a JPK Nanowizard 3 scanning microscope in the contact mode using Si<sub>3</sub>N<sub>4</sub> tips (HYDRA2R-100NG-50, APPNANO), with a spring constant of ~0.011 N m<sup>-1</sup>, a resonance frequency of 21 kHz in air and a tip radius of <10 nm. AFM scanning was conducted in HEPES buffer with a scanning size of 10 × 10 μm, 256 × 256 pixels and a scanning rate of 1 Hz per line<sup>30</sup>. After obtaining the AFM image with the untreated sample, 10 μmol HA was added into the fluid cell and the sample was statically incubated for 20 min, followed by repetition of the aforementioned protocol.

**Statistical analyses and reproducibility.** For determining statistical significance, the *P* value was calculated using permutational multivariate analysis of variance (PERMANOVA) with ADONIS test, two-sided Student's *t*-test or one-way analysis of variance (ANOVA) with Tukey's HSD by SPSS version 24.0 programme. All values are presented as mean ± s.e.m. Experiments were repeated at least three times to confirm reproducibility.

**Reporting summary.** Further information on research design is available in the Nature Research Reporting Summary linked to this article.

## Data availability

The genome sequence of ZJU23, Pa58 has been deposited in the NCBI BioProject database with accession codes PRJNA707237 and PRJNA795028. Raw data of amplicon sequencing, genome sequences of herbicolin A-resistant *S. cerevisiae* mutants and transposon mutants of *P. agglomerans* ZJU23 are deposited in the Genome Sequence Archive of the Beijing Institute of Genomics (BIG) Data Center with accession numbers CRA003916, CRA006594 and CRA006602 in bioproject PRJCA003858 (<https://bigd.big.ac.cn/gsa>). Other data supporting the findings of the present study are available within this article, in Extended Data and the Supplementary Information. Source data are provided with this paper.

## Code availability

Scripts employed in the microbiome analysis are available at <https://github.com/YongxinLiu/WheatFHB>.

Received: 2 April 2021; Accepted: 22 April 2022;

Published online: 26 May 2022

## References

- Cordovez, V., Dini-Andreote, F., Carrion, V. J. & Raaijmakers, J. M. Ecology and evolution of plant microbiomes. *Annu. Rev. Microbiol.* **73**, 69–88 (2019).
- The Human Microbiome Project Consortium. Structure, function and diversity of the healthy human microbiome. *Nature* **486**, 207–214 (2012).
- Trivedi, P., Leach, J. E., Tringe, S. G., Sa, T. & Singh, B. K. Plant-microbiome interactions: from community assembly to plant health. *Nat. Rev. Microbiol.* **18**, 607–621 (2020).
- Duran, P. et al. Microbial interkingdom interactions in roots promote *Arabidopsis* survival. *Cell* **175**, 973–983.e14 (2018).
- Rodrigues, J. L. et al. Conversion of the Amazon rainforest to agriculture results in biotic homogenization of soil bacterial communities. *Proc. Natl Acad. Sci. USA* **110**, 988–993 (2013).
- Lauber, C. L., Ramirez, K. S., Aanderud, Z., Lennon, J. & Fierer, N. Temporal variability in soil microbial communities across land-use types. *ISME J.* **7**, 1641–1650 (2013).
- Lundberg, D. S. et al. Defining the core *Arabidopsis thaliana* root microbiome. *Nature* **488**, 86–90 (2012).
- Chen, T. et al. A plant genetic network for preventing dysbiosis in the phyllosphere. *Nature* **580**, 653–657 (2020).
- Vorholt, J. A., Vogel, C., Carlstrom, C. I. & Muller, D. B. Establishing causality: opportunities of synthetic communities for plant microbiome research. *Cell Host Microbe* **22**, 142–155 (2017).
- Wei, Z. et al. Initial soil microbiome composition and functioning predetermine future plant health. *Sci. Adv.* **5**, eaaw0759 (2019).
- Bahram, M. et al. Structure and function of the global topsoil microbiome. *Nature* **560**, 233–237 (2018).
- Frey-Klett, P. et al. Bacterial-fungal interactions: hyphens between agricultural, clinical, environmental, and food microbiologists. *Microbiol. Mol. Biol. Rev.* **75**, 583–609 (2011).
- Chen, Y. et al. Wheat microbiome bacteria can reduce virulence of a plant pathogenic fungus by altering histone acetylation. *Nat. Commun.* **9**, 3429 (2018).
- Berg, G. Plant-microbe interactions promoting plant growth and health: perspectives for controlled use of microorganisms in agriculture. *Appl. Microbiol. Biotechnol.* **84**, 11–18 (2009).
- Pal, K. K. & Gardner, B. M. Biological control of plant pathogens. *The Plant Health Instructor* <https://doi.org/10.1094/PHI-A-2006-1117-02> (2006).
- Winkelmann, G., Lupp, R. & Jung, G. Herbicolins - new peptide antibiotics from *Erwinia herbicola*. *J. Antibiot.* **33**, 353–358 (1980).
- Aydin, M. et al. Structure elucidation of the peptide antibiotics herbicolin A and herbicolin B. *Liebigs Ann. Chem.* **11**, 2285–2300 (1985).
- Tenning, P., Vanrijnsbergen, R., Zhao, Y. & Joos, H. Cloning and transfer of genes for antifungal compounds from *Erwinia herbicola* to *Escherichia coli*. *Mol. Plant Microbe Interact.* **6**, 474–480 (1993).
- Kempf, H. J., Bauer, P. H. & Schroth, M. N. Herbicolin A associated with crown and roots of wheat after seed treatment with *Erwinia herbicola* B247. *Phytopathology* **83**, 213–216 (1993).
- Kempf, H. J. & Wolf, G. *Erwinia herbicola* as a biocontrol agent of *Fusarium culmorum* and *Puccinia recondita* f. sp. *tritici* on wheat. *Phytopathology* **79**, 990–994 (1989).
- Freundt, E. A. & Winkelmann, G. Activity of herbicolin Aa against *Mycoplasma*, *Acholeplasma*, *Ureaplasma*, and *Spiroplasma* species. *Antimicrob. Agents Chemother.* **26**, 112–114 (1984).
- Dean, R. et al. The top 10 fungal pathogens in molecular plant pathology. *Mol. Plant Pathol.* **13**, 414–430 (2012).
- Trail, F. For blighted waves of grain: *Fusarium graminearum* in the postgenomics era. *Plant Physiol.* **149**, 103–110 (2009).
- Chen, Y., Kistler, H. C. & Ma, Z. *Fusarium graminearum* trichothecene mycotoxins: biosynthesis, regulation, and management. *Annu. Rev. Phytopathol.* **57**, 15–39 (2019).
- Mendes, R. et al. Deciphering the rhizosphere microbiome for disease-suppressive bacteria. *Science* **332**, 1097–1100 (2011).
- Carrion, V. J. et al. Pathogen-induced activation of disease-suppressive functions in the endophytic root microbiome. *Science* **366**, 606–612 (2019).
- Kusstscher, P. et al. Microbiome-driven identification of microbial indicators for postharvest diseases of sugar beets. *Microbiome* **7**, 112 (2019).
- Zachow, C., Grosch, R. & Berg, G. Impact of biotic and abiotic parameters on structure and function of microbial communities living on sclerotia of the soil-borne pathogenic fungus *Rhizoctonia solani*. *Appl. Soil Ecol.* **48**, 193–200 (2011).
- Mulner, P. et al. Microbiota associated with sclerotia of soilborne fungal pathogens – a novel source of biocontrol agents producing bioactive volatiles. *Phytobiomes J.* **3**, 125–136 (2019).
- Zhang, Y. J. et al. High-throughput cultivation and identification of bacteria from the plant root microbiota. *Nat. Protoc.* **16**, 988–1012 (2021).
- Tang, G., Chen, Y., Xu, J. R., Kistler, H. C. & Ma, Z. The fungal myosin I is essential for *Fusarium* toxosome formation. *PLoS Pathog.* **14**, e1006827 (2018).
- Zhang, C. & Seyedsayamost, M. R. Discovery of a cryptic depsipeptide from *Streptomyces ghanaensis* via MALDI-MS-guided high-throughput elicitor screening. *Angew. Chem. Int. Ed.* **59**, 23005–23009 (2020).
- Liu, X., Jiang, J. H., Yin, Y. N. & Ma, Z. H. Involvement of *FgERG4* in ergosterol biosynthesis, vegetative differentiation and virulence in *Fusarium graminearum*. *Mol. Plant Pathol.* **14**, 71–83 (2013).
- Liu, Z. et al. A phosphorylated transcription factor regulates sterol biosynthesis in *Fusarium graminearum*. *Nat. Commun.* **10**, 1228 (2019).
- Rautenbach, M., Troskie, A. M. & Vosloo, J. A. Antifungal peptides: to be or not to be membrane active. *Biochimie* **130**, 132–145 (2016).

36. Song, D. et al. *Pseudomonas aeruginosa* quorum-sensing metabolite induces host immune cell death through cell surface lipid domain dissolution. *Nat. Microbiol.* **4**, 97–111 (2019).
37. Klymchenko, A. S. & Kreder, R. Fluorescent probes for lipid rafts: from model membranes to living cells. *Chem. Biol.* **21**, 97–113 (2014).
38. Takeshita, N., Diallinas, G. & Fischer, R. The role of flotillin FloA and stomatin StoA in the maintenance of apical sterol-rich membrane domains and polarity in the filamentous fungus *Aspergillus nidulans*. *Mol. Microbiol.* **83**, 1136–1152 (2012).
39. Schulz-Bohm, K. et al. Fungus-associated bacteriome in charge of their host behavior. *Fungal Genet. Biol.* **102**, 38–48 (2017).
40. Brown, S. P., Grillo, M. A., Podowski, J. C. & Heath, K. D. Soil origin and plant genotype structure distinct microbiome compartments in the model legume *Medicago truncatula*. *Microbiome* **8**, 139 (2020).
41. Wagner, M. R. et al. Host genotype and age shape the leaf and root microbiomes of a wild perennial plant. *Nat. Commun.* **7**, 12151 (2016).
42. Rosenberg, E. & Zilber-Rosenberg, I. Microbes drive evolution of animals and plants: the hologenome concept. *mBio* **7**, e01395 (2016).
43. Schlaepi, K., Dombrowski, N., Oter, R. G., Ver Loren van Themaat, E. & Schulze-Lefert, P. Quantitative divergence of the bacterial root microbiota in *Arabidopsis thaliana* relatives. *Proc. Natl Acad. Sci. USA* **111**, 585–592 (2014).
44. Spor, A., Koren, O. & Ley, R. Unravelling the effects of the environment and host genotype on the gut microbiome. *Nat. Rev. Microbiol.* **9**, 279–290 (2011).
45. Schmidt, R., Ulanova, D., Wick, L. Y., Bode, H. B. & Garbeva, P. Microbe-driven chemical ecology: past, present and future. *ISME J.* **13**, 2656–2663 (2019).
46. Straight, P. D. & Kolter, R. Interspecies chemical communication in bacterial development. *Annu. Rev. Microbiol.* **63**, 99–118 (2009).
47. Mentges, M. et al. Infection cushions of *Fusarium graminearum* are fungal arsenals for wheat infection. *Mol. Plant Pathol.* **21**, 1070–1087 (2020).
48. Sieber, C. M. et al. The *Fusarium graminearum* genome reveals more secondary metabolic gene clusters and hints of horizontal gene transfer. *PLoS ONE* **9**, e110311 (2014).
49. Kim, J. E. et al. Putative polyketide synthase and laccase genes for biosynthesis of eurofusarin in *Gibberella zeae*. *Appl. Environ. Microbiol.* **71**, 1701–1708 (2005).
50. Pent, M., Bahram, M. & Poldmaa, K. Fruitbody chemistry underlies the structure of endofungal bacterial communities across fungal guilds and phylogenetic groups. *ISME J.* **14**, 2131–2141 (2020).
51. Shade, A. Diversity is the question, not the answer. *ISME J.* **11**, 1–6 (2017).
52. Konopka, A., Lindemann, S. & Fredrickson, J. Dynamics in microbial communities: unravelling mechanisms to identify principles. *ISME J.* **9**, 1488–1495 (2015).
53. Nemergut, D. R. et al. Patterns and processes of microbial community assembly. *Microbiol. Mol. Biol. Rev.* **77**, 342–356 (2013).
54. Grosskopf, T. & Soyer, O. S. Synthetic microbial communities. *Curr. Opin. Microbiol.* **18**, 72–77 (2014).
55. Winkelmann, G., Lupp, R. & Jung, G. Herbicolins—new peptide antibiotics from *Erwinia herbicola*. *J. Antibiot. (Tokyo)* **33**, 353–358 (1980).
56. Buda De Cesare, G., Cristy, S. A., Garsin, D. A. & Lorenz, M. C. Antimicrobial peptides: a new frontier in antifungal therapy. *mBio* **11**, e02123-20 (2020).
57. Song, B., Rong, Y. J., Zhao, M. X. & Chi, Z. M. Antifungal activity of the lipopeptides produced by *Bacillus amyloliquefaciens* anti-CA against *Candida albicans* isolated from clinic. *Appl. Microbiol. Biotechnol.* **97**, 7141–7150 (2013).
58. Tao, Y., Bie, X. M., Lv, F. X., Zhao, H. Z. & Lu, Z. X. Antifungal activity and mechanism of fengycin in the presence and absence of commercial surfactin against *Rhizopus stolonifer*. *J. Microbiol.* **49**, 146–150 (2011).
59. Liu, Y. et al. C16-fengycin A affect the growth of *Candida albicans* by destroying its cell wall and accumulating reactive oxygen species. *Appl. Microbiol. Biotechnol.* **103**, 8963–8975 (2019).
60. Sur, S., Romo, T. D. & Grossfield, A. Selectivity and mechanism of fengycin, an antimicrobial lipopeptide, from molecular dynamics. *J. Phys. Chem. B* **122**, 2219–2226 (2018).
61. Maget-Dana, R. & Peypoux, F. Iturins, a special class of pore-forming lipopeptides: biological and physicochemical properties. *Toxicology* **87**, 151–174 (1994).
62. Denning, D. W. Echinocandin antifungal drugs. *Lancet* **362**, 1142–1151 (2003).
63. Zhang, J. Y. et al. NRT1.1B is associated with root microbiota composition and nitrogen use in field-grown rice. *Nat. Biotechnol.* **37**, 676–684 (2019).
64. Liu, Y. X. et al. A practical guide to amplicon and metagenomic analysis of microbiome data. *Protein Cell* **12**, 315–330 (2020).
65. Caporaso, J. G. et al. QIIME allows analysis of high-throughput community sequencing data. *Nat. Methods* **7**, 335–336 (2010).
66. Bolyen, E. et al. Reproducible, interactive, scalable and extensible microbiome data science using QIIME 2. *Nat. Biotechnol.* **37**, 852–857 (2019).
67. Edgar, R. C. Search and clustering orders of magnitude faster than BLAST. *Bioinformatics* **26**, 2460–2461 (2010).
68. Edgar, R. C. UPARSE: highly accurate OTU sequences from microbial amplicon reads. *Nat. Methods* **10**, 996–998 (2013).
69. Quast, C. et al. The SILVA ribosomal RNA gene database project: improved data processing and web-based tools. *Nucleic Acids Res.* **41**, D590–D596 (2013).
70. Edgar, R. C., Haas, B. J., Clemente, J. C., Quince, C. & Knight, R. UCHIME improves sensitivity and speed of chimer detection. *Bioinformatics* **27**, 2194–2200 (2011).
71. Cole, J. R. et al. Ribosomal database project: data and tools for high throughput rRNA analysis. *Nucleic Acids Res.* **42**, D633–D642 (2014).
72. Chen, T. et al. ImageGP: an easy-to-use data visualization web server for scientific researchers. *iMeta* **1**, e5 (2022).
73. Knights, D. et al. Bayesian community-wide culture-independent microbial source tracking. *Nat. Methods* **8**, 761–763 (2011).
74. Hu, W. A. et al. Potential of *Pseudomonas chlororaphis* subsp. *aurantiaca* strain Pcho10 as a biocontrol agent against *Fusarium graminearum*. *Phytopathology* **104**, 1289–1297 (2014).
75. Qiu, J. G. et al. Biodegradation of picolinic acid by a newly isolated bacterium *Alcaligenes faecalis* strain JQ135. *Curr. Microbiol.* **74**, 508–514 (2017).
76. Zhao, Y. F., Wang, D. P., Nakka, S., Sundin, G. W. & Korban, S. S. Systems level analysis of two-component signal transduction systems in *Erwinia amylovora*: role in virulence, regulation of amylovoran biosynthesis and swarming motility. *BMC Genomics* **10**, 245 (2009).
77. Steinberg, G. et al. A lipophilic cation protects crops against fungal pathogens by multiple modes of action. *Nat. Commun.* **11**, 1608 (2020).
78. Collins, M. D. & Gordon, S. E. Giant liposome preparation for imaging and patch-clamp electrophysiology. *J. Vis. Exp.* **76**, 50227 (2013).
79. Pott, T., Bouvrais, H. & Meleard, P. Giant unilamellar vesicle formation under physiologically relevant conditions. *Chem. Phys. Lipids* **154**, 115–119 (2008).

## Acknowledgements

We thank J. Blodgett (Washington University, St. Louis, USA) and C. Liu (Zhejiang University, China) for herbicolin A biosynthetic gene cluster analysis; Y. Xiao (Chinese Academy of Sciences, China) and F. Xu (Zhejiang University, China) for structural identification of compounds; Q. Wang (Northwest A&F University, China) for analysing transposon insertion sites in the ZJU23 and mutated sites in yeast; and W. Fu (Zhejiang University, China) for the molecular docking analysis. This work was supported by grants from: the Key Technology R&D Program of Zhejiang Province (grant no. 2019C02034) to Z.M.; the National Science Fund for Excellent Young Scholars (grant no. 31922074) to Y.C.; the China Agriculture Research System (grant no. CARS-3-29) to Z.M.; the Strategic Priority Research Program of the Chinese Academy of Sciences (CAS) (grant no. XDA24020104) to Y.B.; and the Youth Innovation Promotion Association CAS (grant no. 2021092) to Y.-X.L.

## Author contributions

Y. Chen and Z.M. initiated, coordinated and supervised the project. S.X., H.W., Y.Z. and Z.W. collected samples and isolated bacterial strains. Y.-X.L., B.Q. and Y.B. performed bacterial community profiling. S.X. and H.W. performed gene knockout experiments. S.X., C.L. and S.C. identified compounds. S.X., T.X., H.R. and Y.S. performed lipid raft experiments. X-X.S. phylogenetically analysed the HA biosynthetic gene cluster. Y. Chen, S.X., Z.M., Y.-X.L. and Y.B. collected and analysed the data. Y. Chen, Z.M., S.X., Y.B., T.C. and Y.Y. wrote the manuscript. Y. Chen, Y. Chai, G.B. and X.Z. revised the manuscript.

## Competing interests

The authors declare no competing interests.

## Additional information

**Extended data** is available for this paper at <https://doi.org/10.1038/s41564-022-01131-x>.

**Supplementary information** The online version contains supplementary material available at <https://doi.org/10.1038/s41564-022-01131-x>.

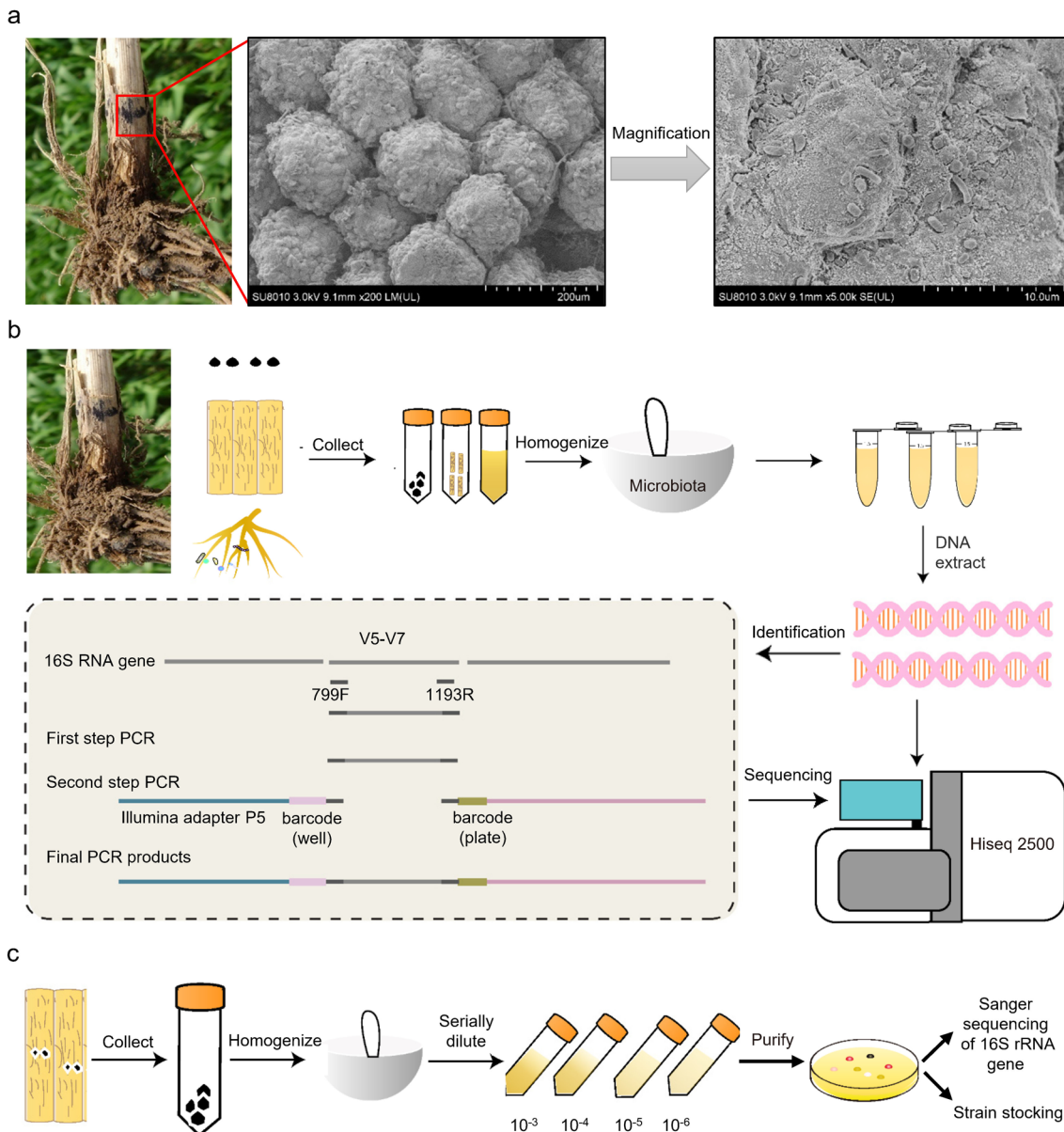
**Correspondence and requests for materials** should be addressed to Yunlong Yu, Yang Bai or Yun Chen.

**Peer review information** *Nature Microbiology* thanks Marcio Rodrigues and the other, anonymous, reviewer(s) for their contribution to the peer review of this work. Peer reviewer reports are available.

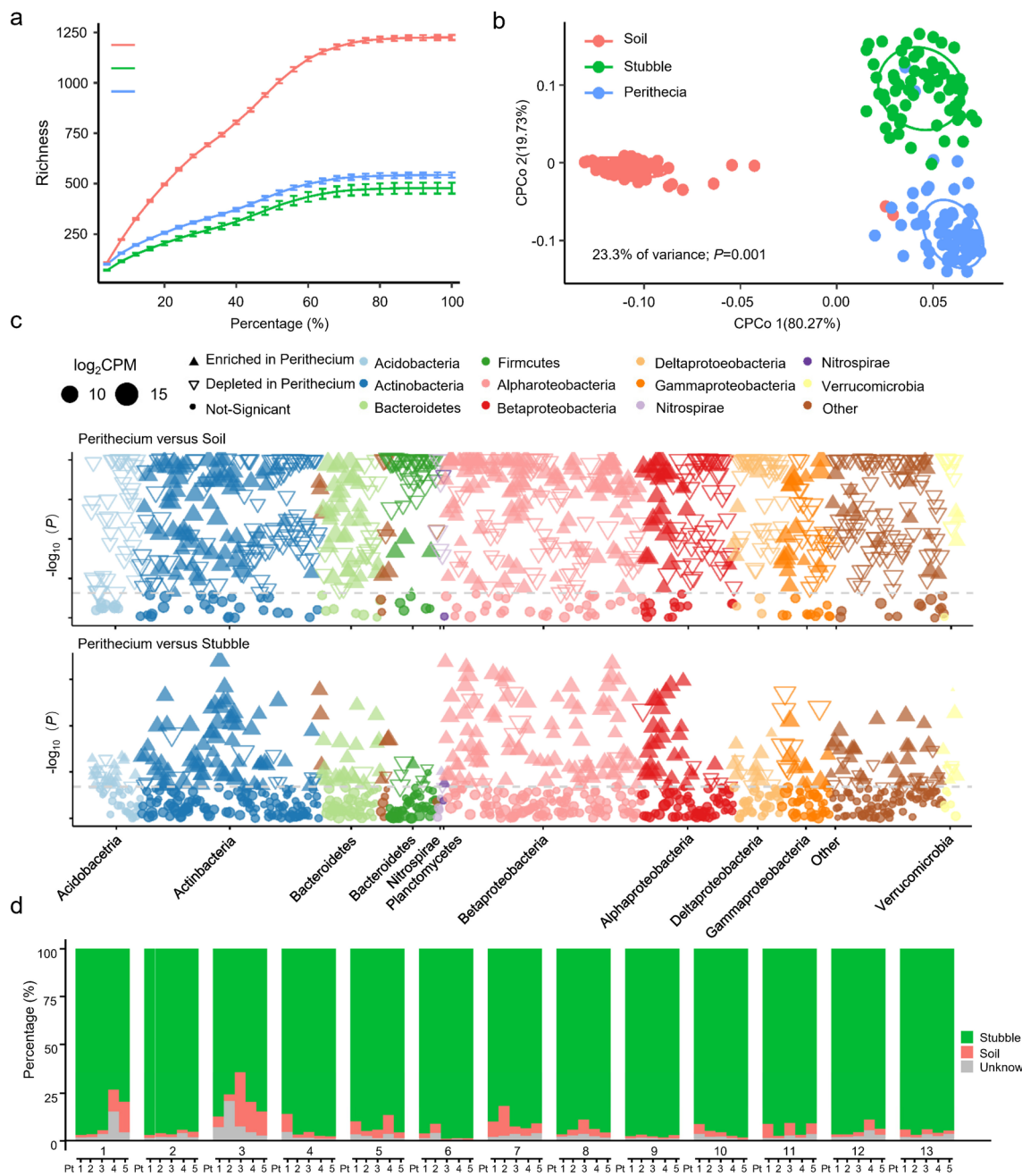
**Reprints and permissions information** is available at [www.nature.com/reprints](http://www.nature.com/reprints).

**Publisher's note** Springer Nature remains neutral with regard to jurisdictional claims in published maps and institutional affiliations.

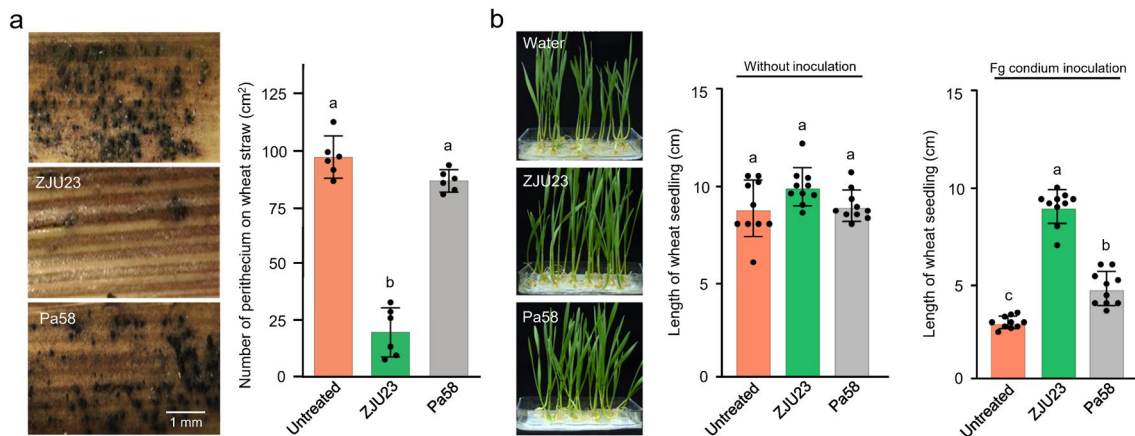
© The Author(s), under exclusive licence to Springer Nature Limited 2022



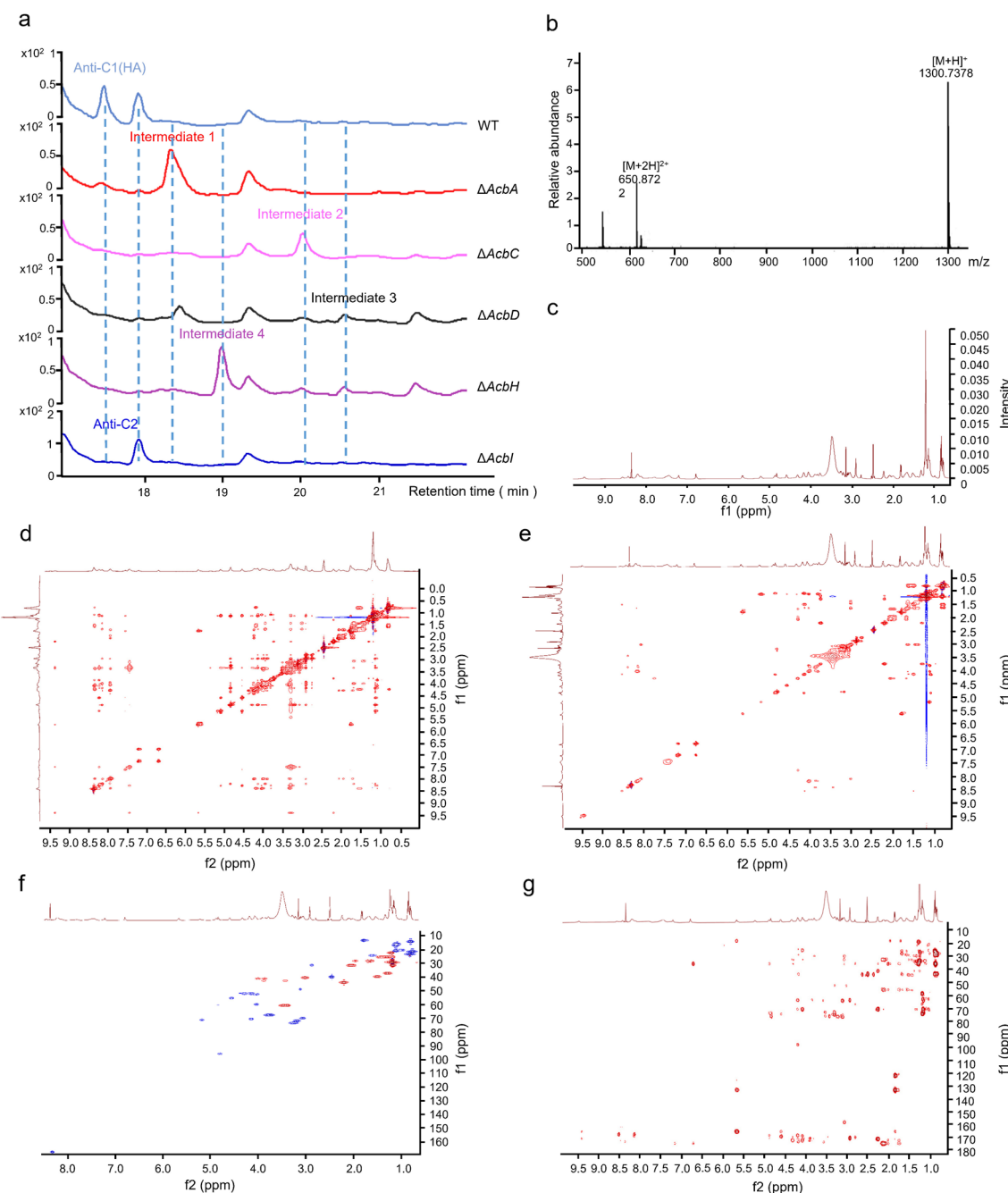
**Extended Data Fig. 1 | Experimental procedure for assessing perithecia-associated bacterial communities.** **a**, Collection of perithecia and microscopic visualization of bacteria on the surface of perithecia using a scanning electron microscope. The experiment was repeated five times with similar results. **b, c**, Experimental procedure used to analyse the detailed analysis of the peritheciun-associated microbiome and the corresponding cultivable bacterial isolates. Bacterial identification procedure was modified from Zhang et al., 2019<sup>63</sup>.



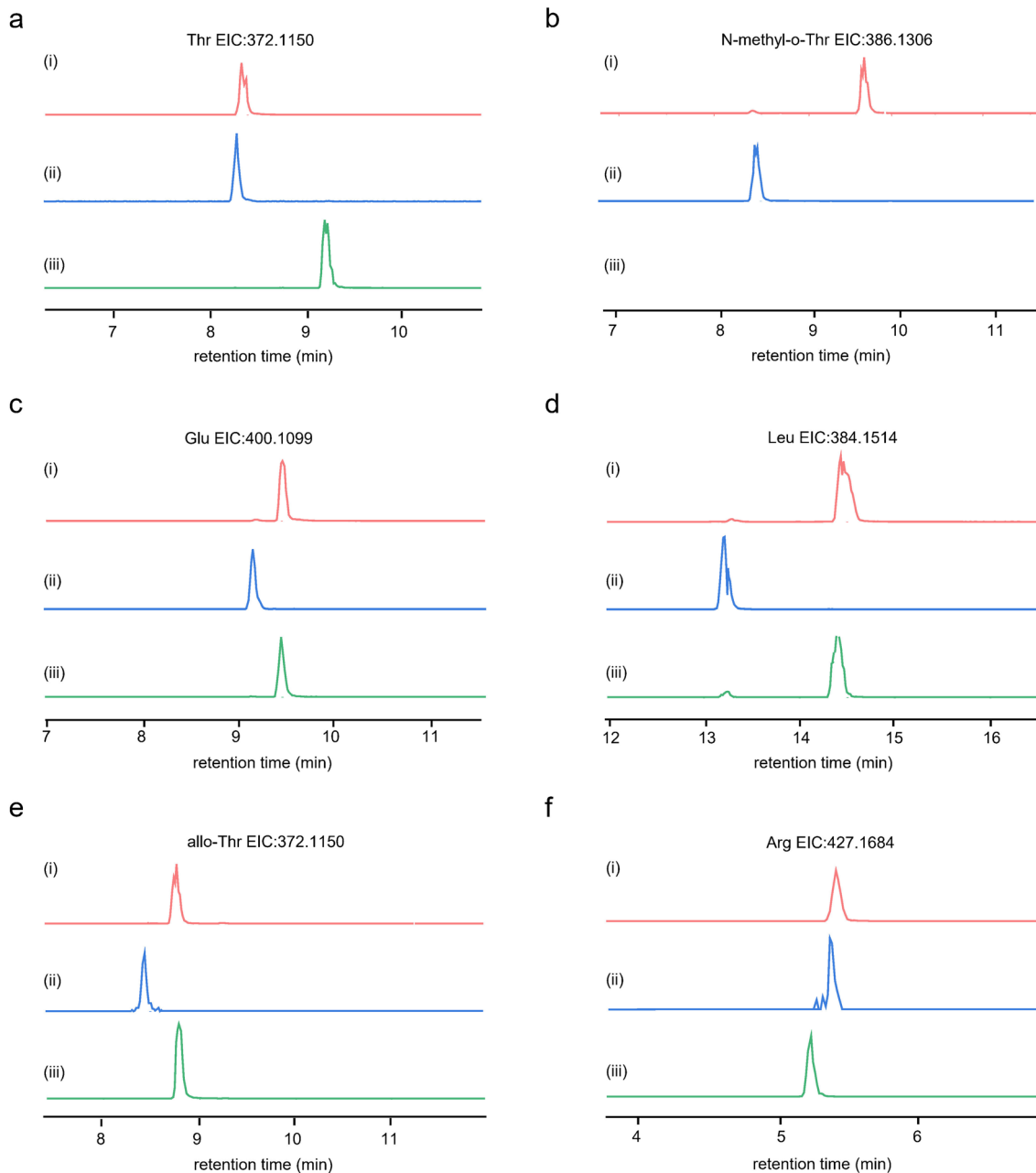
**Extended Data Fig. 2 | Diversity and differential abundance of OTUs in the peritheciuum, stubble and soil samples.** **a**, Rarefaction curves of detected bacterial OTUs in microbiomes from each compartment. The saturation stage with increasing numbers of sequencing reads indicates that bacterial diversity was sufficiently covered by the implemented approach. The richness index of peritheciuum, stubble and soil samples is shown separately (mean  $\pm$  s.e.m.). **b**, Constrained principal coordinate analysis (CPCoA) of Bray-Curtis dissimilarity showing compartment effects on the microbial community structure. Ellipses cover 68% of the samples for each compartment. **c**, Manhattan plot showing OTUs that were enriched or depleted in peritheciuum versus soil and stubble. Each dot or triangle represents a single OTU. OTUs enriched or depleted in peritheciuum samples are represented by filled or empty triangles, respectively (FDR adjusted  $P < 0.001$ , Wilcoxon rank-sum test). OTUs are arranged in taxonomic order and colored according to their phylum and the proteobacteria class. CPM, counts per million. Numbers of replicated samples for each compartment,  $n = 65$  biologically independent samples. **d**, Source analysis of average peritheciuum compartment attribution using SourceTracker trained on the stubble and soil microbiome datasets. Replicates for each compartment,  $n = 65$  biologically independent samples.



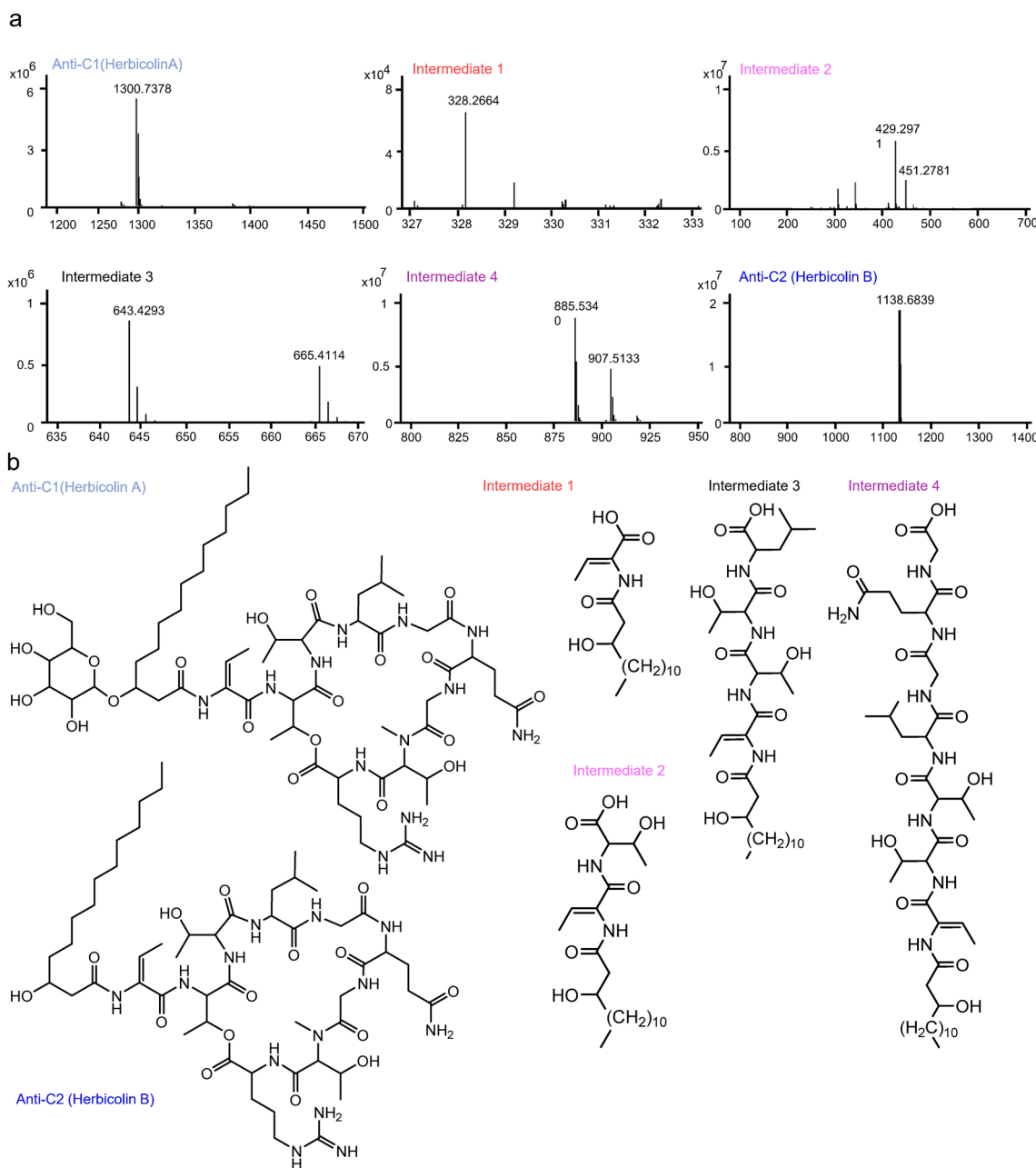
**Extended Data Fig. 3 | ZJU23 inhibitory effects on the formation of *Fg* perithecia on rice straws and the length of wheat seedlings in each treatment with or without conidial of *Fg*.** **a**, *Fg* peritheciun formation in different treatments on rice straws. Images were taken after 14 days post-inoculation (dpi) from  $n=6$  biologically independent samples (mean  $\pm$  s.e.m.). Different letters indicate significantly different groups ( $P < 0.05$ , ANOVA, Tukey HSD). The non-antagonistic *P. agglomerans* Pa58 strain was used as a control. The experiment was repeated three times with similar results. **b**, The length of wheat seedlings with or without *F. graminearum* (*Fg*) inoculation in each treatment are shown at 7 dpi. The length of the wheat seedlings at 7 dpi was measured and statistically analyzed ( $n=10$  biologically independent seedlings for each treatment, mean  $\pm$  s.e.m.). Different letters indicate significantly different groups ( $P < 0.05$ , ANOVA, Tukey HSD). Representative wheat seedlings without *Fg* inoculation in each treatment are shown. The experiment was repeated three times with similar results.



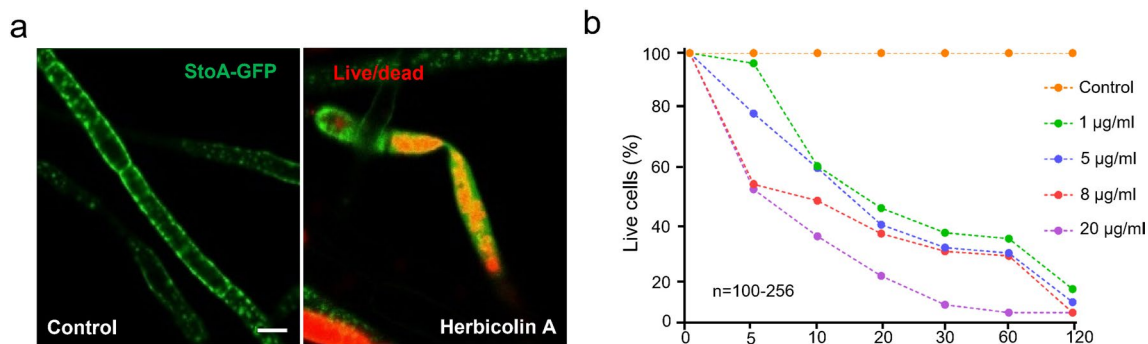
**Extended Data Fig. 4 | Purification and identification of herbicin A.** **a**, Comparative total ion flow diagram profile between ZJU23 and deletion mutants in the HA biosynthetic gene cluster. **b**, High-resolution mass spectra (HRMS) of herbicin A showing a peak at  $m/z$  1300.7378, which corresponds to the  $[M+H]^+$  ion and another at  $m/z$  650.8722, which corresponds to the  $[M+2H]^{2+}$  ion. **c**,  $^1\text{H}$  NMR spectrum of HA. **d**, NOESY NMR spectrum. **e**, TOCSY NMR spectrum. **f**,  $^1\text{H}$ - $^{13}\text{C}$  HSQC NMR spectrum. **g**,  $^1\text{H}$ - $^{13}\text{C}$  HMBC NMR spectrum.



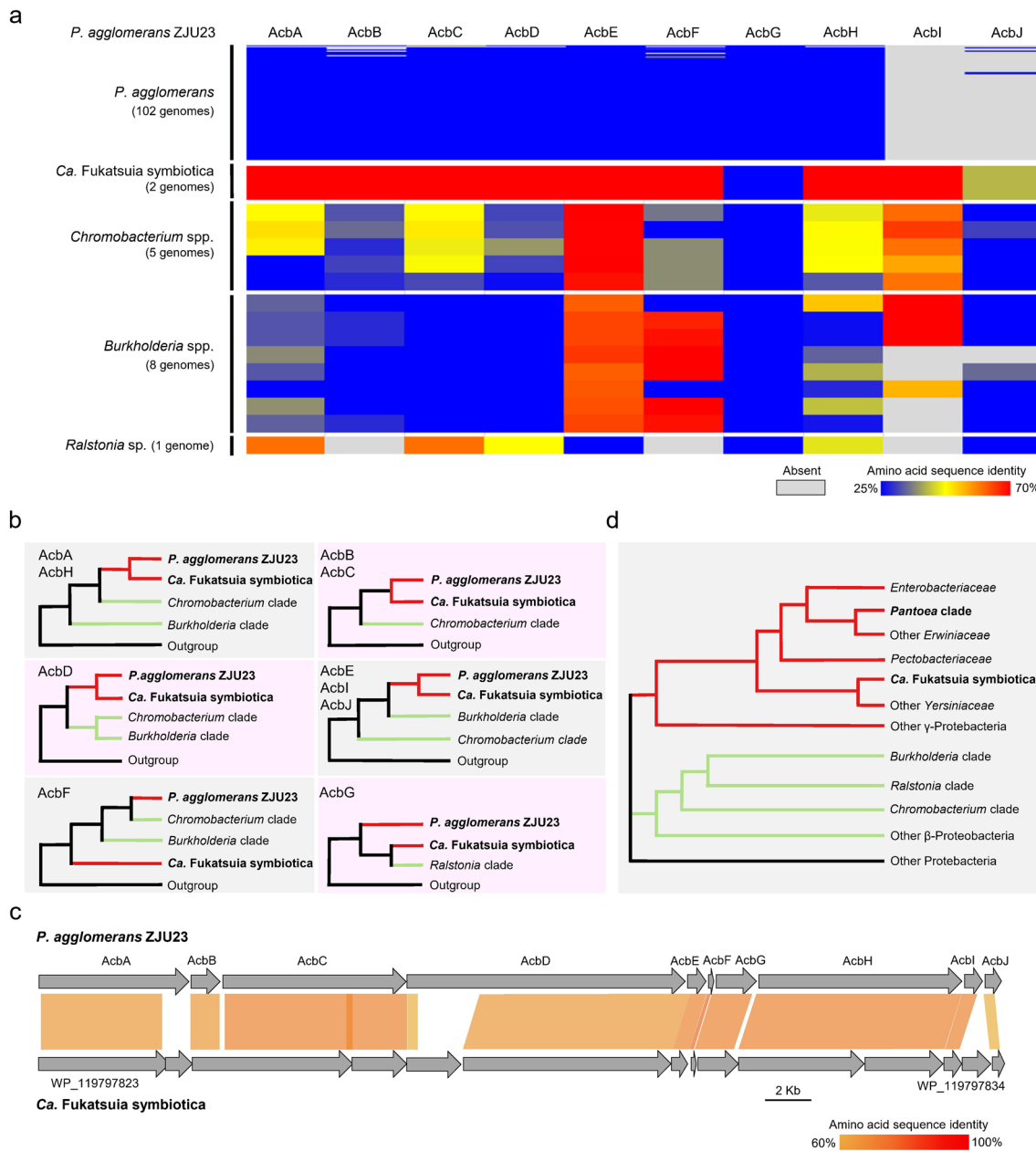
**Extended Data Fig. 5 | Stereochemistry of Thr (a), N-Methy-Thr (b), Glu (c), Leu (d), allo-Thr (e) and Arg (f) residues in herbicolin A determined by Marfey's method.** Shown are extracted ion chromatograms of amino acid-FDAA adducts detected by HPLC-Qtof-MS of hydrolyzed, FDAA-derivatized herbicolin A and the amino acid standards. (i) herbicolin A-L-FDAA; (ii) L-AA-L-FDAA; (iii) D-AA-L-FDAA. FDAA, 1-fluoro-2-4-dinitrophenyl-5-L-alanine amide.



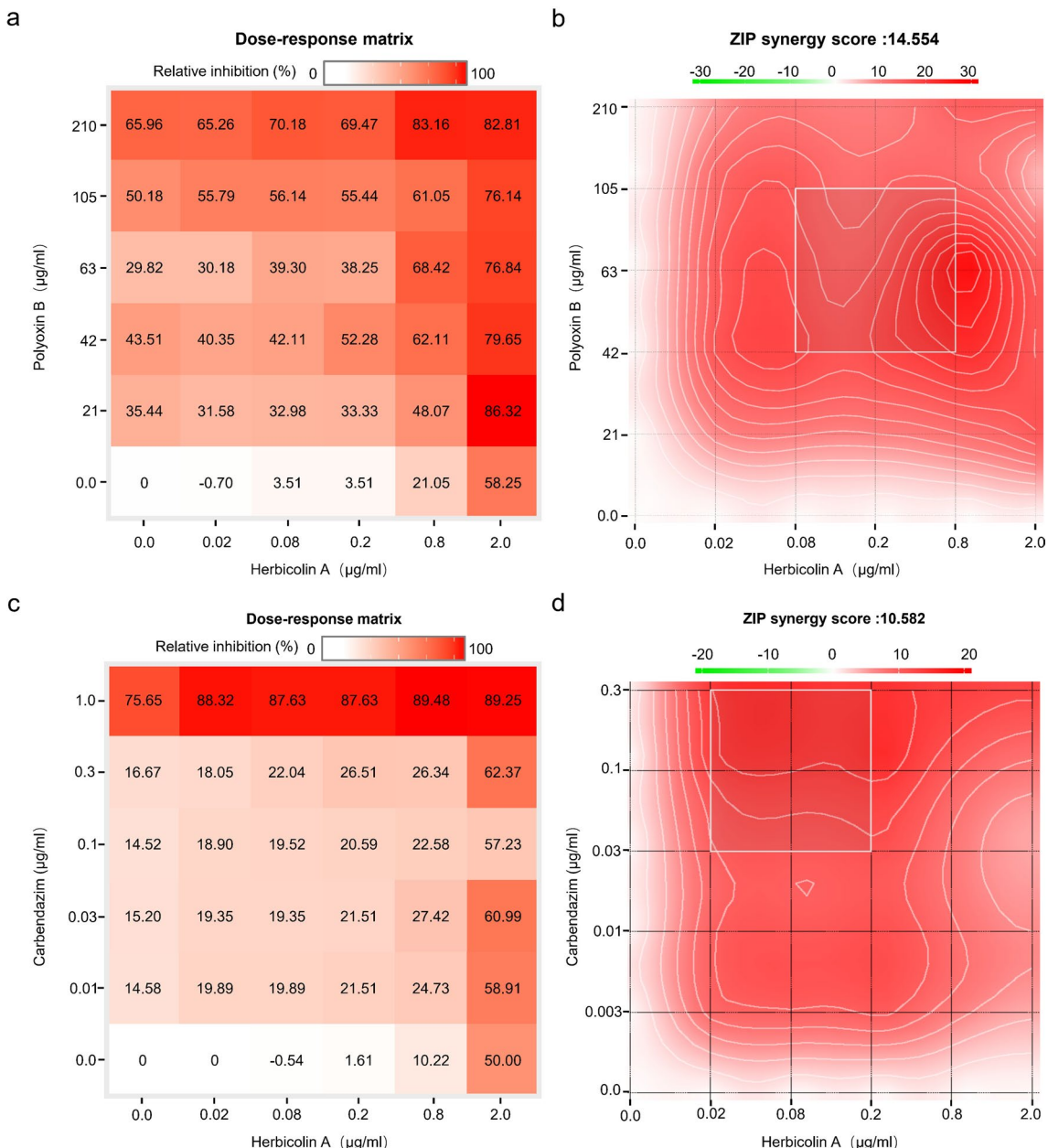
**Extended Data Fig. 6 | Structures of intermediates in the herbicin A biosynthesis.** **a**, Electrospray ionization spectra of herbicin A, herbicin B, intermediate 1–4. **b**, Structures of herbicin A, herbicin B, intermediate 1–4.



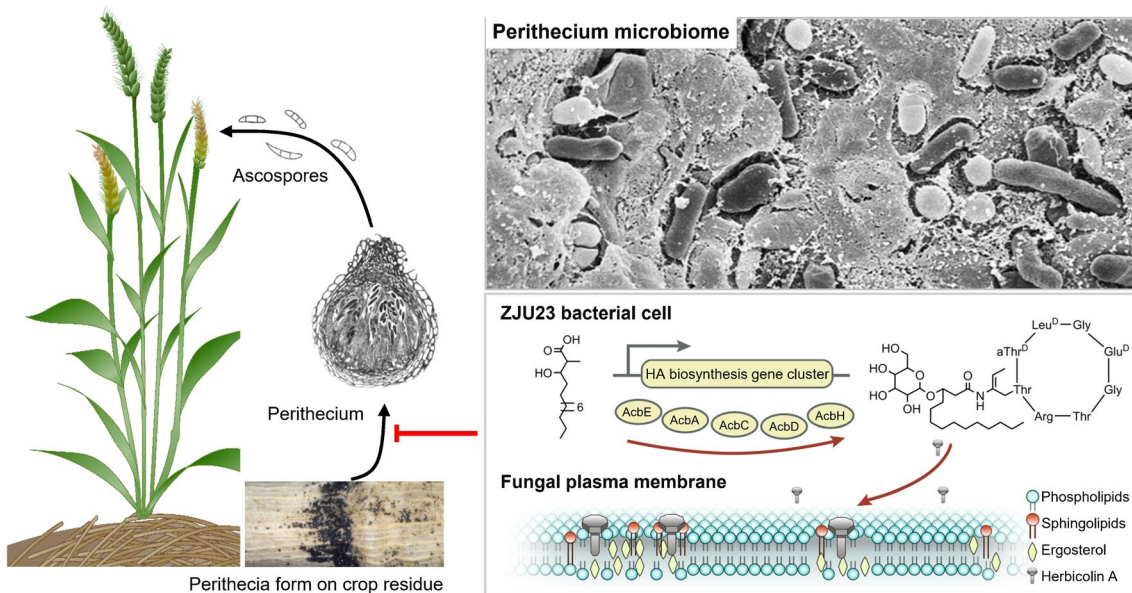
**Extended Data Fig. 7 | Growth inhibition of HA in various concentrations towards *Fg* mycelia in agar plates.** **a**, Live/dead staining of *F. graminearum* cells expressing the plasma membrane marker GFP-StoA, after treatment with HA. Dead cells are indicated by either yellow or red staining. Scale bar, 5 μm. The experiment was repeated five times with similar results. **b**, Survival curves of *F. graminearum* cells grown in liquid medium supplemented or not (Control) with the indicated concentrations of HA. Data presented the mean ± s.e.m.. The experiment was repeated five times with similar results.



**Extended Data Fig. 8 | Origin of the herbicolin A biosynthetic cluster in ZJU23.** **a**, Heatmap representation of the amino acid identities (%) of individual HA biosynthetic proteins shared between ZJU23 and other tested strains. **b**, Phylogenies of the 10 genes in the cluster correspond to six different patterns. Specific genes supporting each of the patterns are listed on top. **c**, Microsynteny and amino acid sequence conservation between the HA biosynthesis cluster in ZJU23 and a predicted gene cluster in *Ca. Fukatsuia symbiotica*. The hits between the two clusters are indicated with different shades of yellow, and the identity scale (45–100%) is included. **d**, Phylogenetic tree of tested bacterial species.  $\gamma$ -Proteobacteria,  $\beta$ -Proteobacteria and other proteobacteria are indicated with red, green and black lines.



**Extended Data Fig. 9 | Synergistic effects between herbicolin A and two tested fungicides, polyoxin B and carbendazim.** Two-dimensional matrix of dose-response for relative mycelial growth inhibition of *F. graminearum* in the combinations of herbicolin A and polyoxin B (**a**), and herbicolin A and carbendazim (**c**). Synergyfinder was used to generate a topographic two-dimensional map of synergy scores for the combination of herbicolin A and polyoxin B (**b**), herbicolin A and carbendazim (**d**), respectively. Synergistic and antagonistic dosage zones are highlighted in red and green on the synergy map, respectively. The area with the greatest synergy score is indicated by a white box.



**Extended Data Fig. 10 | Proposed model for the mode of action of herbicolin A, which is secreted by ZJU23 in the peritheciatum microbiome, on *Fusarium graminearum*.** The biocontrol bacterium *P. agglomerans* ZJU23 was isolated from *F. graminearum* peritheciatum microbiome. ZJU23 showed strong in vitro and in situ antagonism, which was later attributed to the secreted antifungal compound herbicolin A (HA). The HA biosynthetic gene cluster AcbA-J was obtained via horizontal gene transfer from *Candidatus Fukatsuia* symbiotica. HA binds ergosterol and disrupts the integrity of ergosterol-containing fungal lipid rafts, which subsequently suppresses fungal growth, substantially reducing peritheciatum formation and virulence of *F. graminearum*.

## Reporting Summary

Nature Portfolio wishes to improve the reproducibility of the work that we publish. This form provides structure for consistency and transparency in reporting. For further information on Nature Portfolio policies, see our [Editorial Policies](#) and the [Editorial Policy Checklist](#).

### Statistics

For all statistical analyses, confirm that the following items are present in the figure legend, table legend, main text, or Methods section.

n/a Confirmed

- The exact sample size ( $n$ ) for each experimental group/condition, given as a discrete number and unit of measurement
- A statement on whether measurements were taken from distinct samples or whether the same sample was measured repeatedly
- The statistical test(s) used AND whether they are one- or two-sided  
*Only common tests should be described solely by name; describe more complex techniques in the Methods section.*
- A description of all covariates tested
- A description of any assumptions or corrections, such as tests of normality and adjustment for multiple comparisons
- A full description of the statistical parameters including central tendency (e.g. means) or other basic estimates (e.g. regression coefficient) AND variation (e.g. standard deviation) or associated estimates of uncertainty (e.g. confidence intervals)
- For null hypothesis testing, the test statistic (e.g.  $F$ ,  $t$ ,  $r$ ) with confidence intervals, effect sizes, degrees of freedom and  $P$  value noted  
*Give P values as exact values whenever suitable.*
- For Bayesian analysis, information on the choice of priors and Markov chain Monte Carlo settings
- For hierarchical and complex designs, identification of the appropriate level for tests and full reporting of outcomes
- Estimates of effect sizes (e.g. Cohen's  $d$ , Pearson's  $r$ ), indicating how they were calculated

*Our web collection on [statistics for biologists](#) contains articles on many of the points above.*

### Software and code

Policy information about [availability of computer code](#)

Data collection	No software was used.
Data analysis	Software packages for 16S amplicon data included EasyAmplicon v1.09, QIIME v1.9.1, QIIME 2 v2020.11, and USEARCH10 v11.0.667's UPARSE and UCHIME algorithm. Databases for 16S amplicon data included RDP train set 16, SILVA 132. We used R v4.0.3 and SPSS v24 for statistical analyses. We used R 4.0.3 (including ggplot2 v2.3.2, and ggtree v2.2.4), GraPhlAn v.0.9.7 and imageGP for plotting. GraphPad Prism version 5.01 was used for producing bar chart and growth curves. Scripts employed in the computation analyses are available in <a href="https://github.com/YongxinLiu/WheatFHB">https://github.com/YongxinLiu/WheatFHB</a> .

For manuscripts utilizing custom algorithms or software that are central to the research but not yet described in published literature, software must be made available to editors and reviewers. We strongly encourage code deposition in a community repository (e.g. GitHub). See the Nature Portfolio [guidelines for submitting code & software](#) for further information.

### Data

Policy information about [availability of data](#)

All manuscripts must include a [data availability statement](#). This statement should provide the following information, where applicable:

- Accession codes, unique identifiers, or web links for publicly available datasets
- A description of any restrictions on data availability
- For clinical datasets or third party data, please ensure that the statement adheres to our [policy](#)

The genome sequence of ZJU23, Pa58 has been deposited in the NCBI BioProject databases with accession codes PRJNA707237 and PRJNA795028. Raw data of amplicon sequencing, genome sequences of herbicoline A-resistant *S. cerevisiae* mutants and transposon mutants of *P. agglomerans* ZJU23 are deposited in the Genome Sequence Archive of Beijing Institute of Genomics (BIG) Data Center with accession number CRA003916, CRA006594 and CRA006602 in BioProject

## Field-specific reporting

Please select the one below that is the best fit for your research. If you are not sure, read the appropriate sections before making your selection.

- Life sciences       Behavioural & social sciences       Ecological, evolutionary & environmental sciences

For a reference copy of the document with all sections, see [nature.com/documents/nr-reporting-summary-flat.pdf](https://nature.com/documents/nr-reporting-summary-flat.pdf)

## Life sciences study design

All studies must disclose on these points even when the disclosure is negative.

Sample size	No sample size calculation was performed. Sample sizes were chosen based on the Authors' experience of what is necessary to generate a convincing and compelling result.
Data exclusions	No data were excluded from our analyses.
Replication	In a parallel experiment, we set up triple replications for determining the mean value and standard deviation. All attempts at replication were successful. All the experiments were conducted at three times to verify the reproducibility.
Randomization	Samples were randomly allocated into experimental groups. The samples of perithecia, soil and stubble were randomly collected.
Blinding	Blind testing was not routinely carried out in this study because it was not relevant to most of the experiments carried out and these were based on molecular genetic and natural product characteristics of HA on Fusarium graminearum, thus requiring knowledge of samples to be processed. Blind testing of virulence phenotypes was carried out as an independent check of phenotypes, wherever possible, such as the information provided in Figure 2f-g and Figure 6d-6f.

## Reporting for specific materials, systems and methods

We require information from authors about some types of materials, experimental systems and methods used in many studies. Here, indicate whether each material, system or method listed is relevant to your study. If you are not sure if a list item applies to your research, read the appropriate section before selecting a response.

### Materials & experimental systems

- n/a Involved in the study
- Antibodies
- Eukaryotic cell lines
- Palaeontology and archaeology
- Animals and other organisms
- Human research participants
- Clinical data
- Dual use research of concern

### Methods

- n/a Involved in the study
- ChIP-seq
- Flow cytometry
- MRI-based neuroimaging

## Animals and other organisms

Policy information about [studies involving animals; ARRIVE guidelines](#) recommended for reporting animal research

### Laboratory animals

ICR mouse were obtained from Zhejiang Center of Laboratory Animals, Hangzhou, Zhejiang. These mice were bred and housed per approved protocols at Laboratory animal room of Hangzhou medial college [SYXL(ZHE)2016-0022]. Sample size for all mice experiments were determined by the minimal number of mice that is able to achieve significant results. Sexually unbiased, 8-12week old of mice were used in this study, . All mouse experiments were subject to randomization.

### Wild animals

this study did not involve wild animals.

### Field-collected samples

this study did not involve samples collected from the field

### Ethics oversight

Institutional Animal Care and Use Committee, ZJCLA

Note that full information on the approval of the study protocol must also be provided in the manuscript.